

Revision of two-temperature magnetically arrested flows onto a black hole

M. Mościbrodzka¹

¹Department of Astrophysics/IMAPP, Radboud University, P.O. Box 9010, 6500 GL Nijmegen, The Netherlands

ABSTRACT

We revisit the radiative properties of 3D general relativistic magnetohydrodynamics (GRMHD) two-temperature magnetically arrested disk (MAD) models in which electrons are heated by a magnetic turbulent cascade. We focus on studying the model emission, whose characteristics include variability in both total intensity and linear/circular polarizations as well as rotation measures at energies around the synchrotron emission peak in millimeter waves. We find that the radiative properties of MAD models with turbulent electron heating are well converged with respect to the numerical grid resolution, which has not been demonstrated before. We compare radiation from two-temperature simulations with turbulent heating to single-temperature models with electron temperatures calculated based on the commonly used $R(\beta)$ prescription. We find that the self-consistent two-temperature models with turbulent heating do not significantly outperform the $R(\beta)$ models and, in practice, may be indistinguishable from the $R(\beta)$ models. Accounting for physical effects such as radiative cooling and the nonthermal electron distribution function makes a weak impact on properties of millimeter emission. Models are scaled to Sgr A*, an accreting black hole in the center of our galaxy, and compared to the most complete observational datasets. We point out the consistencies and inconsistencies between the MAD models and observations of this source and discuss future prospects for GRMHD simulations.

Keywords: Supermassive black holes (1663), Magnetohydrodynamical simulations (1966), Low-luminosity active galactic nuclei (2033), Plasma physics (2089)

1. INTRODUCTION

Magnetically arrested disks (hereafter MADs) are a class of black hole accretion solutions initially developed for radiatively inefficient accretion flows (RIAFs; Iぐmenshchev et al. 2003; Narayan et al. 2003, 2022; Proga & Begelman 2003; Tchekhovskoy et al. 2011; McKinney et al. 2012). In MADs realized in general relativistic magnetohydrodynamics (GRMHD) simulations, the magnetic field flux accumulated near the black hole event horizon is extreme, which has two important consequences. First, the power of jets produced in MAD simulations is significant, which makes the jet opening angle rather large ($\sim 55^\circ$; Chael et al. 2019). This is consistent with what is observed in sub-Eddington accreting black hole systems such as M87 (Kim et al. 2018; Walker et al. 2018). MADs near the black hole horizon are further supported in M87 by the first polarimetric images

from the Event Horizon Telescope (EHT; Event Horizon Telescope Collaboration et al. 2021). Second, the jet magnetosphere in MADs is often reconnecting at the equatorial plane of the simulation causing magnetic field flux eruptions into the disk body. Such flux eruptions have been proposed to explain the flaring behavior of another sub-Eddington accreting supermassive black hole, Sgr A* (Dexter et al. 2020b; Porth et al. 2021; Wielgus et al. 2022b). It has also been recently found that horizon-scale polarimetric images of Sgr A* are more consistent with MADs (Event Horizon Telescope Collaboration et al. 2024). Although less magnetized standard and normal evolution accretion disks (SANEs), or wind-fed accretion or tilted-disk models (e.g., Ressler et al. 2019; Chatterjee et al. 2020), are not completely ruled out by observations of any of the sources, the MAD RIAF solution became a leading candidate to explain the observations of the two best-resolved aforementioned accreting supermassive black holes.

One of the most uncertain parts of MADs (but also SANEs) is how they generate emission. In the aforementioned class of systems, where the accreting plasma

Corresponding author: M. Mościbrodzka
 m.moscibrodzka@astro.ru.nl

is collisionless, electron and ion distribution functions remain unknown. Typically, to mimic the collisionless effects in models, we assume that the plasma has two-temperature structure, and we “paint” electron temperatures on the top of the GRMHD models according to some parameterized law. An example of such a parameterized law for the thermal distribution of electrons is the $R(\beta)$ prescription of Mościbrodzka et al. 2016 used in Event Horizon Telescope Collaboration et al. 2022, where the model parameter $R(\beta) \equiv T_i/T_e(\beta)$ is a ratio of the nonemitting ion to the emitting electron temperatures that depends on the local plasma $\beta (\equiv P_{\text{mag}}/P_{\text{gas}})$ parameter. Other than the $R(\beta)$ models have been proposed by Mościbrodzka & Falcke (2013); Mościbrodzka et al. (2014); Chan et al. (2015); Gold et al. (2017); Anantua et al. (2020). Alternatively, one can assume a nonthermal electron distribution function, but those are typically also parametric (see, e.g., Davelaar et al. 2018; Cruz-Osorio et al. 2022; Fromm et al. 2022; Scepi et al. 2022; Zhao et al. 2023 for recent work and Chael et al. 2017; Petersen & Gammie 2020 for examples of models with evolution of nonthermal electrons). Finally, one can model two-temperature GRMHD flows where electron temperatures are followed by a separate equation that includes nonadiabatic (viscous), subgrid heating terms based on plasma or particle-in-cell considerations (Howes 2010; Rowan et al. 2017; Kawazura et al. 2019) and radiative cooling terms (e.g., Ryan et al. 2018).

The method of tracking electron temperatures in GRMHD simulations assuming a subgrid model for ion and electron heating has been introduced by Ressler et al. (2015). Sadowski et al. (2017) further developed the idea to add the ion/electron pressure as well as a self-consistent variable adiabatic index to the GRMHD evolution. Two-temperature 2D and 3D GRMHD models have been carried out in the past, specifically for Sgr A* (Ressler et al. 2017; Sadowski et al. 2017; Chael et al. 2018; Dexter et al. 2020a; Jiang et al. 2023) and M87 (Ryan et al. 2018; Mizuno et al. 2021; Dihingia et al. 2023).

In this paper, we revisit the two-temperature GRMHD MAD simulations. The mentioned previous studies used several numerical codes assuming various torus sizes, magnetic field topologies, adiabatic indices, and grid resolutions to investigate the problem. It was not clear to us that the radiative output of these models is converged for MAD models with setups comparable to those in the EHT simulation library (Event Horizon Telescope Collaboration et al. 2022). The second motivation for the revision of two-temperature simulations is the fact that MAD models with $R(\beta)$ prescription typically have too-

variable total intensity compared to the observations of Sgr A* (Event Horizon Telescope Collaboration et al. 2022; Wielgus et al. 2022a). The origin of the discrepancy between the models and the observations is unknown. One possibility is that the $R(\beta)$ model, which was initially developed for SANE simulations, is not suitable for MADs, and a more sophisticated electron model should be adopted. One could also ask how physically motivated the $R(\beta)$ model is for electron temperatures when considering MADs. The latter is relevant for all sub-Eddington-accreting black hole systems. Finally, the measurement of black hole spin in EHT and other sources is typically accretion-model-dependent. A robust understanding of the dissipation processes in accreting plasma near the event horizon is critical for reliable spin estimates.

In this work, we investigate how the numerical model parameters impact the radiative (total intensity and polarimetric) characteristics of the two-temperature MAD simulations. We first demonstrate that they are independent of the grid resolution used in GRMHD simulations. Next, we evolve models for longer times and compare the two-temperature models with $R(\beta)$ models. Finally, having checked that the results are weakly dependent on the exact shape of the electron distribution function and that they remain unchanged even when radiative cooling is introduced (scaling models to the Sgr A* system), we compare the prograde and retrograde two-temperature MAD models to the newest multifrequency polarimetric millimeter observational data of Sgr A*. In contrast to most of the previous two-temperature simulations, in our comparisons, we focus on variability and polarization, which together are significantly more informative than the time-averaged or total intensity comparisons. We discuss the future prospects for investigating the thermodynamics of the GRMHD simulations.

The paper is structured as follows. In Section 2 we describe our 3D two-temperature GRMHD simulations setups and outline the details of radiative transfer modeling. In Section 3, we report the results and compare the models with selected observations of Sgr A*. We discuss the results and conclude in Section 4.

2. MODELS

2.1. GRMHD simulations

MAD simulations are carried by means of `ebhlight`, a radiative GRMHD code developed and made public by Ryan et al. (2015). `ebhlight` is a relativistic, second-order, conservative, constrained-transport code for stationary spacetimes. While the fluid part of the code is based on the `harm` routines (Gammie et al. 2003), the ra-

diation part is based on `grmonty` scheme (Dolence et al. 2009).

All simulations are set in geometrized units where the length scale and time scale are set by the black hole mass: $\mathcal{L} \equiv GM/c^2$ and $\mathcal{T} \equiv GM/c^3$ (assuming $G = c = 1$ both time and distance are measured in units of mass, M). The simulations start from the Fishbone-Moncrief torus (Fishbone & Moncrief 1976) at the equatorial plane of a Schwarzschild or Kerr black hole. The torus is described by two parameters: inner radius $r_{\text{in}} = 20M$ and radius of the pressure maximum $r_{\text{max}} = 41M$. The torus is seeded with weak poloidal magnetic fields described by vector potential,

$$(A_r, A_\theta, A_\phi) = (0, 0, \frac{\rho}{\rho_{\text{max}}} \left(\frac{r}{r_{\text{in}}} \right)^3 \exp \left(\frac{r}{r_0} \right) \sin^3 \theta - 0.2) \quad (1)$$

where r, θ are the radius and polar angle in Kerr-Schild coordinates, parameter $r_0 = 400M$, ρ is the plasma density. The initial magnetic field is renormalized so that plasma $\beta_{\text{max}} = 100$.

The simulations use ideal equation of state with constant adiabatic index of $\gamma_{ad} = 13/9$; i.e., we assume that plasma is pure hydrogen with nonrelativistic protons and relativistic electrons for which adiabatic indices are $\gamma_p = 5/3$ and $\gamma_e = 4/3$, respectively.

All simulations are carried out in mixed modified Kerr-Schild logarithmic coordinates, where the resolution is focused on the equatorial plane and toward the central region close to the black hole horizon. The grid stretches from within the black hole event horizon until $r_{\text{out}} = 1000M$.

The grid refinement convergence test runs are integrated for 10,000M assuming four grid resolutions listed in Table 1. Convergence runs are performed for black hole spin $a_* = 0$. Later in the paper, we consider both prograde and retrograde fiducial models (also listed in Table 1) with the following spin values: $a_* = -0.9375, -0.5, 0, 0.5, 0.9375$. The prograde and zero-spin models are evolved until 30,000M, and the retrograde models are evolved for a shorter time, only until 14,000M. In all our simulations, the accretion flows reach steady state within $r = 20M$. Fiducial models have grid resolutions $(N_r, N_\theta, N_\phi) = (240, 120, 128)$ (for $a_* = -0.5, 0, 0.5$) and $(N_r, N_\theta, N_\phi) = (266, 120, 128)$ (for $a_* = -0.9375, 0.9375$). All models above are run with radiative modules of `ebhlight` turned off. We carry out one test run with radiative effects turned on. The parameters of the exploratory radiative GRMHD (GRRMHD) model are shown in Table 1.

2.2. Radiative transfer

We measure the convergence of the models by studying their radiative properties. To predict synchrotron emission from the simulations, we postprocessed the GRMHD snapshots using the ray-tracing relativistic polarized radiative transfer code `ipole` (Mościbrodzka & Gammie 2018). The radiative transfer calculations are typically carried out starting at later times of simulations when the accretion flow is relaxed from the initial conditions (starting times, t_s , and final times, t_f , of all radiative transfer postprocessing simulations are listed in Table 1). We scale all GRMHD simulations using the mass and distance of the Sgr A* black hole. The models density scale is set by unit \mathcal{M} , a standard mass or accretion rate \dot{M} scaling factor (e.g., $\rho_{Sgr\ A*} = \mathcal{M}/\mathcal{L}^3 \rho_{\text{code}}$). In all models \mathcal{M} is set to produce an average Sgr A* total flux of 2-3 Jy observed at a frequency of 229 GHz (Wielgus et al. 2022a). Table 1 lists each model \mathcal{M} and corresponding \dot{M} . Given the electron temperature model (see next subsection), the imaging code produces synchrotron emission maps at a desired frequency ν (here 86–229 GHz) and a viewing angle i . Initially, all maps are computed for a default viewing angle $i = 160^\circ$ selected based on the recent rediscovery of a transient hot spot orbiting around Sgr A* (Wielgus et al. 2022b, see also viewing angle estimates by Yfantis et al. 2024) and then later for additional viewing angles $i = 150^\circ, 130^\circ, 110^\circ$. Note that for the modeled source, lower viewing angles are favored by EHT observations that revealed a symmetric ring (Event Horizon Telescope Collaboration et al. 2022); hence we do not model emission for high viewing angles, $i \sim 90^\circ$. Assuming $i > 90^\circ$ also guarantees the correct sign of the circular polarization for the assumed polarity of magnetic fields in the GRMHD models. Our model map resolution is 256×256 pixels and the field of view = $120M \approx 600 \mu\text{as}$. A time series of maps/images with a cadence of $\Delta t = 10M$ is synthesized into light curves in Stokes I, Q, U, V . Following Wielgus et al. 2022a the modulation index $M_3 \equiv \sigma_{\Delta T}/\mu_{\Delta T}$ (ratio of standard deviation to mean flux calculated on time intervals $\Delta T = 3$ hr) is used to characterize light-curve variability in Stokes I at two frequencies, 86 and 229 GHz. We also calculate the spectral index in total intensity (α_I between 213 and 229 GHz), (Faraday) rotation measure (RM; between 213 and 229 GHz), and linear (LP) and circular (CP) fractional polarizations at 86 and 229 GHz. These particular quantities are studied because they are later compared directly to observations. In our models Faraday rotation is caused by relativistic and subrelativistic electrons within 100M from the event horizon; these electrons constitute the so-called internal Faraday screen.

2.3. Electron distribution functions

Following the scheme of Ressler et al. (2015), the `ebhlight` code tracks total and electron entropies that are used to calculate the nonadiabatic (viscous) gas heating rates and evolve electron temperatures. The scheme requires the provision of a subgrid model for the proton-to-electron heating ratio Q_p^+/Q_e^+ . In this work, we adopt the prescription for Q_p^+/Q_e^+ developed by Kawazura et al. (2019, henceforth model K), which approximates dissipation in a turbulent cascade with a functional form

$$\frac{Q_p^+}{Q_e^+} = \frac{35}{1 + (\beta/15)^{-1.4} \exp^{-0.1T_e/T_p}}. \quad (2)$$

In this model, most of the dissipation goes to protons in high β plasma regions, while electrons receive most of the heating in low β regions. Qualitatively and quantitatively, the K model is very similar to the turbulent heating model of Howes (2010). Studying significantly different options for Q_p^+/Q_e^+ , such as, for example, electron heating by reconnection (Rowan et al. 2017), is beyond the scope of the current paper but is discussed in Section 4.

In ideal GRMHD models studied here using a conservative code, the total viscous heating is produced by truncation errors at the numerical grid level. One may conclude that no matter what fraction of this heating goes to the electrons, this heating will be completely artificial. However, for the turbulent torus problem, the grid-scale dissipation is set by the large-scale turbulence in the problem (see Section 3.1 in Ressler et al. 2015 for a more detailed discussion). The numerical scheme for electron heating implemented in `ebhlight` has been carefully tested against some analytic problems by Ressler et al. (2015) and Ryan et al. (2017) as well as Sadowski et al. (2017), who, except for the mentioned modifications, follow the same idea when evolving electron temperatures alone. We are not going to repeat these tests here. In `ebhlight` the electron evolution also does not include Coulomb couplings, unless radiative transfer is activated (see Section 3.2.1). However, those are not important in the low-density gas considered here. In `ebhlight` the electron temperature tracking is passive; i.e. the electron pressure is not accounted for in the GRMHD equations. More importantly, the heating of the proton (nonadiabatic/viscous) is not taken into account in the GRMHD equations as well; instead, the internal energy of the gas is evaluated from the total energy using an inversion scheme implemented in the code assuming γ_{ad} . The proton temperatures are computed using the total internal energy u , the plasma density ρ , and $\gamma_p = 5/3$ ($\Theta_p \equiv (\gamma_p - 1)u/\rho$).

The simulations are two-temperature, but to make a connection with the previous studies, we use the same GRMHD runs and compute images/light curves using a parametric electron temperature model $R(\beta)$. In this model, proton temperatures are calculated from GRMHD quantities, and the electron temperature is found using the formula below:

$$R(\beta) \equiv \frac{T_p}{T_e} = R_{\text{high}} \frac{\beta^2}{1 + \beta^2} + R_{\text{low}} \frac{1}{1 + \beta^2}, \quad (3)$$

where parameters R_{low} and R_{high} are temperature ratios that describe the proton-to-electron temperature ratio in strongly (low plasma β) and weakly (high plasma β) magnetized regions, respectively. To be consistent with Event Horizon Telescope Collaboration et al. (2022, 2024), we calculate the light curves for $R_{\text{high}} = 1, 10, 40, 160$ and $R_{\text{low}} = 1$. The dimensionless electron temperature that is passed to the synchrotron transfer coefficients in `ipole` is calculated from

$$\Theta_e = \frac{u m_p}{\rho m_e} \frac{(\gamma_p - 1)(\gamma_e - 1)}{(\gamma_e - 1)R + (\gamma_p - 1)} \quad (4)$$

with internal energy u and rest-mass density ρ provided by GRMHD model. The electron model assumes $\gamma_e = 4/3$ and $\gamma_p = 5/3$, self-consistent with GRMHD simulations in which electrons are relativistic and protons are nonrelativistic.

Models with the Kawazura et al. (2019) prescription for Q_p^+/Q_e^+ are tagged K, and models with parametric electron temperatures are labeled R1-R160 (e.g., model with $R_{\text{low}} = 1$ and $R_{\text{high}} = 160$ is denoted R160). The latter models are referred to as $R(\beta)$ models.

It is reasonable to assume that the energy from the turbulent heating is used to form a nonthermal rather than purely thermal electron distribution function. We consider an exploratory nonthermal model using the $f_\kappa(\gamma, \kappa, w)$ distribution function (Xiao 2006):

$$f_\kappa(\gamma, \kappa, w) = N \gamma \sqrt{\gamma^2 - 1} \left(1 + \frac{\gamma - 1}{\kappa w} \right)^{-(\kappa+1)} \quad (5)$$

where κ and w are parameters and N is the normalization constant. The distribution parameter

$$w = \frac{(\kappa - 3)}{\kappa} \Theta_e, \quad (6)$$

where Θ_e is calculated from the electron entropy in exactly the same manner as in purely thermal K models (see Ressler et al. 2015). Equation 6 states that the entire turbulent energy is distributed into the κ function. The parameter κ is globally constant. Inspired by the solar wind studies, we assume $\kappa = 4.25$ (e.g., Livadiotis et al. 2018). In ray-tracing, the radiative transfer

coefficients for the κ distribution function are adopted from Mościbrodzka & Gammie (2024). No cutoff is applied to the κ distribution function at high energies because it makes a negligible difference when modeling (sub)millimeter emission.

All radiative transfer simulations are carried out only in regions where $\sigma < \sigma_{\text{cut}} = 1$ (where magnetization parameter $\sigma \equiv 2P_{\text{mag}}/pc^2$). This is a standard procedure to avoid modeling emission from near-vacuum jet regions in the GRMHD model where the proton and electron temperatures are inaccurate (e.g., Event Horizon Telescope Collaboration et al. 2022). However, the millimeter emission from regions with $\sigma > 1$ is small, as already shown by Dexter et al. (2020a, see their Appendix D).

2.4. Effects of grid resolution

Table 1 lists four test two-temperature MAD models $a_* = 0$ carried out at different numerical resolutions. Figure 1 shows the equatorial cuts through the four models at the final integration time, $t_f = 10,000\text{M}$. Figure 2 displays the corresponding lightcurves for Stokes I , RM, LP, and CP calculated for the time interval between 5000M and 10,000M at three observing frequencies assuming the K model for electron temperatures. In Figure 2, the bottom panels display a comparison of the M_3 , RM, LP, CP distributions at 229 GHz as a function of grid resolution. There is a very good agreement between the M_3 , RM, LP and CP distributions. Although not shown, this is also true for two other neighboring frequencies of 86 and 690 GHz at which the modeled source could be observed.

We conclude that the results presented in the remainder of this work do not strongly depend on the chosen GRMHD grid resolution. Around the current level of resolution, which is typically used for building EHT GRMHD model libraries, all the modeled quantities are rather settled, and the small variations in observables are due to different realizations of turbulence in individual runs¹. We note that we cannot exclude that our models are located at the resolution plateau and that increasing resolution 10 times in each direction may result in the simulation better resolving more physical effects (e.g., better resolution of shocks and reconnection layers may lead to different electron heating in different regions of the flow) that could lead to quantitative and qualitative changes in the emission properties.

3. RESULTS

¹ Turbulence is always initialized by a random perturbation of the gas internal energy.

3.1. Turbulent heating vs. ($R(\beta)$) model

The parameters of all the fiducial runs are summarized in Table 1. Figure 3 shows an example of snapshots from our fiducial two-temperature MAD $a_* = 0.9375$ simulation. The fiducial lightcurves produced by the GRMHD simulations with different parameters are presented in Appendix A and here we discuss distributions of quantities calculated based on these lightcurves.

Figure 4 displays the correlations of the observables in models R1 - 160 and K for the default viewing angle $i = 160^\circ$, combined for black hole spins $a_* = 0, 0.5, 0.9375$. In the M_3 panels, the K models are moderately correlated with the R1 - 160 models, and the K models are generally less variable compared to models R1 - 160. The spectral slope α_I and CP in model K are highly correlated with those of model R10. This is not the case for RM and LP, for which the correlation is much weaker.

Figure 5 shows the comparison of the distributions of the observables for the models shown in Figure 4. The averages of M_3 , LP, and CP (and standard deviations) in model K are weakly distinguishable from those of models R1 - 160.

It is useful to look at the properties of the maps used to synthesize the integrated observables. Figure 6 shows examples of EHT-like images at 229 GHz produced by a random snapshot of the $a_* = 0.5$ simulation with R1, R10, R40, R160 and K electron models for the fiducial viewing angle of $i = 160^\circ$. Following Event Horizon Telescope Collaboration et al. 2024 we characterize these images using the following metrics. Net LP and CP are defined as

$$m_{\text{net}} \equiv \frac{\sqrt{(\sum_i Q_i)^2 + (\sum_i U_i)^2}}{\sum_i I}, v_{\text{net}} \equiv \frac{\sum_i V_i}{\sum_i I_i}. \quad (7)$$

The image-averaged LP and CP are defined as

$$m_{\text{avg}} \equiv \frac{\sum_i \sqrt{Q_i^2 + U_i^2}}{\sum_i I_i}, v_{\text{avg}} \equiv \frac{\sum_i |V_i/I_i| I_i}{\sum_i I_i}, \quad (8)$$

where sums are carried out over all image pixels. The geometry of LP is described with amplitudes and phases of a complex function,

$$\beta_m \equiv \frac{\int_0^\infty \int_0^{2\pi} P(\rho, \phi) e^{-im\phi} \rho d\phi d\rho}{\int_0^\infty \int_0^{2\pi} I(\rho, \phi) \rho d\phi d\rho} \quad (9)$$

where

$$P(\rho, \phi) \equiv Q(\rho, \phi) + iU(\rho, \phi) \quad (10)$$

is the complex polarization vector and ρ, ϕ are the polar coordinates in the image plane (see Palumbo et al. 2020 or Event Horizon Telescope Collaboration et al. 2024

for details). All these metrics are shown in the example snapshot in Figure 6. Here, it is more evident that the resolved images of model K are most similar to model R10 in both LP and CP. Model R1 differs from K in CP maps. Models R40 - 160 already have a distinct appearance compared to model K in both LP and CP, as also evident from the comparison of integrated CP. When scored against existing or future (total intensity or polarimetric) EHT data, model K may favor similar accretion flow and geometrical parameters as model R10.

It is important to show that the T_p/T_e in the K models does not precisely follow the R (β) model R10, regardless of the fact that Q_p^+/Q_e^+ is strongly dependent on β . An example of T_p/T_e maps for a single snapshot of the MAD model with high spin is shown in Figure 7 (top and middle panels). The discrepancy between T_p/T_e in models R10 and K indicates that there is no simple relationship between Q_p^+/Q_e^+ and T_p/T_e as already shown by Ressler et al. (2015) for non-MAD models. Hence, the exact electron temperature consistency is not the main reason behind the similarity of K and R10 models. The difference in T_p/T_e between the models is the smallest close to the black hole, and it increases with radius. The emitting regions close to the black hole have on average $T_p/T_e = 10$. The R10 and K models therefore share the scaling unit \mathcal{M} to reproduce the same flux, meaning that ρ and B in the synchrotron radiative transfer coefficients are identical, leading to similar images. The differences between the model's emissions reflect differences in Θ_e (shown in the bottom panels of Figure 7) and seem small from the observational point of view. Due to the Faraday rotation effects, LP and RM are the most sensitive among our observables to electron temperatures at small and larger radii. This explains the weaker correlation of LP and RM between the R10 and K models visible in Figure 4.

3.2. Importance of other physical effects

3.2.1. Effects of radiative cooling

We perform a GRRMHD simulation of the MAD $a_* = 0$ model to check the impact of radiative cooling on electron temperatures and emission properties. The radiative processes included in the GRRMHD simulation include synchrotron emission, self-absorption, Compton scatterings, and bremsstrahlung. To reduce the large computational cost of models with activated multifrequency radiative transfer, the interactions between the photon field and the gas are allowed only within 100M. Any radiative transfer effects outside of this sphere are negligible. When producing emission, the code takes into account the fact that the combined

four-momentum of gas and radiation has to be conserved. Emission/absorption/scattering can therefore exert force on the gas and change the electron thermodynamics (radiative cooling or heating). In the models considered here, the average optical thickness of the gas is $\tau \ll 1$ and luminosities are strongly sub-Eddington, $L \ll L_{\text{Edd}}$; hence, it is expected that in models with activated radiative transfer, mainly electron thermodynamics is affected and mainly due to synchrotron cooling. Other effects are weak for the accretion rates considered. In Appendix B, we present quality factors for the GRRMHD simulation to demonstrate that the interactions between gas and radiation are resolved by an adequate number of Monte Carlo samples.

Figure 8 displays volume-averaged radial profiles of density, magnetic field, T_p/T_e (or R), and Θ_e in the GRMHD and GRRMHD model with the K heating mechanism and $\mathcal{M} = 5 \times 10^{11}$ at different time moments, earlier and later in the evolution. All quantities are additionally weighed by the ρB factor to show quantities averaged over the regions where most of the synchrotron emission comes from (the ρB factor is a major factor in synchrotron emissivity; see, e.g. Pandya et al. 2016 and their Eq. 24 or Eq. 29). There is a small difference in the radial profiles Θ_e and R in models with and without radiative effects, and the difference is due to the different realization of turbulence in each model. Unsurprisingly, at later times in both models, $R \sim 10$ for $r < 20M$, consistent with the results in Section 3.1. Figure 9 shows that there is no difference in radiative characteristics between the GRMHD (K) and GRRMHD (Kcool) models based on $15,000 - 30,000M$ light curves. The total 230 GHz flux of model K averaged over the above time period is 2.99 and 2.93 Jy in models with and without radiative effects, respectively. This suggests that the radiating models simply do not cool fast enough to significantly affect the electron temperatures. This is expected considering very small accretion rates onto Sgr A*.

Since the test model with cooling has the highest \mathcal{M} among all K models considered in this work (see Table 1), all other K models shown in the paper are expected to cool down even slower than the test case. Radiative cooling effects in MADs with turbulent heating may be neglected when modeling Sgr A* millimeter emission.

3.2.2. Effects of nonthermal electrons

Figure 10 shows the comparison of the observational characteristics of thermal and nonthermal K fiducial runs. Non-thermal models are slightly less variable compared to the thermal models. The spectral slope α_I and the RM and the LP of both thermal and nonthermal

models are strongly correlated (the correlation is much stronger compared to the $R(\beta)$ models). It is evident that the total intensity and LP are not sensitive to details of the distribution function for the considered part of the electromagnetic spectrum. CP, on the other hand, is different in both models; hence it may be used to discriminate between distribution functions. We note that CP is usually a more permissive observational constraint compared to LP (see, e.g., [Event Horizon Telescope Collaboration et al. 2024](#)). Overall, with the exception of CP, all radiative properties of our simple nonthermal models are tightly correlated with their purely thermal counterparts.

3.3. Fiducial models vs. ALMA constraints

Having checked how the results depend on numerical resolution effects and the two most relevant physical effects, we can now compare the thermal two-temperature models directly to observations of plasma around Sgr A*.

Figure 11 shows the comparison of the prograde models K, at various viewing angles, to Sgr A* observables detected by the Atacama Large Millimeter/submillimeter Array (ALMA) at 86 and 213 - 229 GHz in 2017, April ([Wielgus et al. 2022a,b, 2024](#)). The modulation index at both frequencies increases with black hole spin and inclination angle. In general, all models are too variable to match the observed variability (this is also the case for the R1 - 160 models found in [Event Horizon Telescope Collaboration et al. 2022](#) and shown here in Figure 5), but the data strongly favor lower spins at lower inclination angles, for which M_3 is the smallest. All models are too optically thin when compared to observations (as is also the case for the R1 - 160 models; compare our Figure 5 with Figure 12, and see also [Ricarte et al. 2023](#)). All models also require an external Faraday screen to explain the observations of RM, but we notice that models with low viewing angles ($i = 160^\circ, 150^\circ$) best recover the RM standard deviation toward the source. LP of the $i = 160^\circ - 150^\circ$ models is consistent with both 229 and 86 GHz measurements. Models with $a_* = 0$ recover CP at 229 GHz but fail to recover CP at 86 GHz. On the other hand, models with $a_* = 0.9375$ fail to recover CP at 229 GHz, but do recover CP at 86 GHz. Only the model with $a_* = 0.5$ does reasonably well with regard to CP at both frequencies. It is possible that a model with a black hole spin in between 0 and 0.5 would be a better fit to the ALMA CP data. Among prograde MADs, the model with $a_* = 0.5$ is the closest to the ALMA observations overall.

Although turbulence in the retrograde models reached a quasi-stationary state within the emission zone, they

are reported separately because they are integrated over shorter times compared to the prograde models. Figure 12 compares the statistical properties of the light curves produced by retrograde MADs. The two-temperature MAD with $a_* = -0.5$ performs better compared to MAD $a_* = -0.9375$ as they are less variable, but worse than MAD $a_* = 0.5$, because prograde models better recover CP at both frequencies.

4. DISCUSSIONS

In this work, we have carried out several two-temperature MAD simulations with the main purpose of investigating the impact of various numerical parameters on the emission properties of these models, in particular grid resolution, but we also investigate the impact of physical effects.

Regarding numerical parameters, the two-temperature MAD simulations with turbulent heating of electrons are well converged with respect to the GRMHD grid resolution in agreement with the only published emission convergence test based on non-MAD models ([Ressler et al. 2017](#)).

Regarding physical parameters, radiative cooling can be safely omitted in Sgr A* two-temperature MAD models with turbulent heating, as radiative effects do not significantly affect the electron temperature evolution. These effects may be important when modeling M87, which is a brighter source. We have also carried out the first exploratory survey of models in which turbulent heating is dissipated into a nonthermal electron distribution function. Our nonthermal models display very similar characteristics compared to the thermal models. However, including the physics of nonthermal electrons in the emission models slightly decreases the model variability and alters the CP compared to purely thermal models. Other, also spatially variable parameters of the κ distribution function could be considered and change our result (e.g., [Davelaar et al. 2019](#)).

Long-duration two-temperature simulations indicate that the thermal models of K are only roughly approximated with the R10 models. Using total intensity observables, [Mizuno et al. \(2021\)](#) found that the best match to turbulent heating models are R5 models. Given that their electron temperatures are defined differently (compare their Eq. 8 with our Eq. 4) and are a factor of ~ 2 smaller than ours, the best match with R10 found here is consistent with the previous finding.

In Section 3.3 we show that none of our long-duration two-temperature K simulations recover the general properties of light curves of Sgr A* observed by ALMA ideally, but the ALMA data favor models with lower viewing angles $i = 150^\circ - 160^\circ$ for which the variabilities

of Stokes I and RM are the smallest. All models have great difficulty recovering the observed model spectral index, in excellent agreement with the previous two-temperature study by Dexter et al. 2020a. All models recover the observed net LP but require the introduction of an additional external Faraday screen to recover the observed RM. Only the $a_* = 0.5$ model recovers Sgr A* net CP at two observed frequencies simultaneously, and it is possible that a spin between 0 and 0.5 would produce even better results. The preferred moderate/low spin value is consistent with spin estimates based on two-temperature models of Dexter et al. 2020a, although for different than the turbulent heating scenario, different initial conditions, and different observational datasets. Here we also study the evolution of two-temperature MADs for low and high spins for a significantly longer time compared to Dexter et al. 2020a.

It is possible that ALMA observes varying compact emission together with less varying extended emission that is not captured in our simulations (C.F. Gammie 2025, private communication); hence, it is preferable to compare models with EHT images (or best with the future EHT movies) rather than integrated quantities. Compared to EHT data, the K models are expected to favor a parameter space similar to the R10 models. Polarimetric EHT data of Sgr A* have not yet ruled out all MAD R10 models. In fact, 10 out of 20 MAD models passing are R10 models (see Fig. 8 in Event Horizon Telescope Collaboration et al. 2024). Based on the similarity between the appearance of R10 and K, we argue that the turbulent electron heating scenario could still be consistent with the observations of Sgr A*. It is interesting to note that in Event Horizon Telescope Collaboration et al. 2024, MAD model R10 is favored for a set of intermediate viewing angles ($i = 150^\circ - 110^\circ$) and positive and negative spin values. K models could narrow the range of these two geometric parameters.

Based on joint total intensity and polarimetric EHT data, the current best-bet MAD model for Sgr A* is R160, not R10 (Event Horizon Telescope Collaboration et al. 2024). We should discuss the present results in the context of other models for Q_p^+/Q_e^+ . As shown by Dexter et al. (2020a) assuming the Howes (2010) turbulent heating model for Q_p^+/Q_e^+ , there is a negligible difference in the MAD electron temperatures compared to the Kawazura et al. (2019) model. The reconnection Q_p^+/Q_e^+ model of Rowan et al. 2017, on the other hand, may result in slightly lower (but also around R10) electron temperatures with weaker plasma- β dependency (Dexter et al. 2020a; Mizuno et al. 2021). Lower electron temperatures could make the MAD models optically thicker and less varying (Chan et al. 2024), thus push-

ing them toward the right direction, but this remains to be thoroughly examined. Weaker dependence on β in models with reconnection heating can result in more disklike emission of MADs than disk/jetlike emission (Chael et al. 2018), making it more difficult to explain the nearly flat radio spectrum of Sgr A* (Mościbrodzka & Falcke 2013). The radio spectral slope dependency on Q_p^+/Q_e^+ should be carefully checked with high-resolution (jet-resolving) two-temperature MAD models. However, whichever Q_p^+/Q_e^+ scenario above (or a combination of scenarios) is selected, the two-temperature MAD models will have difficulty in naturally developing R160-like electron temperatures near the event horizon. Assuming that MAD is present in the Sgr A* system, this may suggest that $R(\beta)$ models are inappropriate for MADs (we briefly discuss prospects on how to resolve this issue in Appendix C). Alternatively, comparisons of instantaneous model snapshots with time-averaged EHT images synthesized from the time-varying EHT data sets so far (see Event Horizon Telescope Collaboration et al. 2022, 2024) may be introducing some bias in the inference of the electron temperature parameter.

Our simulations are run with constant adiabatic index $\gamma_{\text{ad}} = 13/9$, which is not a self-consistent assumption in regions where electrons are mildly or subrelativistic. Recent simulations of Narayan et al. (2022) suggest that the MAD dynamics is not affected by the choice of γ_{ad} . It is unclear how different, or varying, γ_{ad} alters the discussed total intensity and polarimetric radiative properties of two-temperature MADs. This topic should be investigated in the future.

The recent manuscript by Salas et al. (2024), which was posted after this paper was submitted, models Sgr A* variability in total intensity with two-temperature $a_* = 0.94$ MAD models combining reconnection heating, varying γ_{ad} index, and radiative cooling. Although we agree with their statement that the physical two-temperature models are typically less variable compared to the $R(\beta)$ models (via M_3 characteristics; see our Figure 5, second top panel), further detailed comparisons of our results to Salas et al. (2024) are difficult due to different assumptions in electron heating model, equation of state, and radiative cooling methodology. Interestingly, Salas et al. (2024) models, as ours, still do not produce variability fully consistent with the observational data of Wielgus et al. (2022a).

The ideal GRMHD models considered here do not include many other potentially important effects. Additional physics, such as resistivity (e.g., Vos et al. 2024), viscosity, plasma composition (Emami et al. 2021; Wong & Gammie 2022), anisotropic pressures (e.g., Foucart et al. 2017), or anisotropic electron distribution func-

tions (e.g., Galishnikova et al. 2023), may all impact the radiative characteristics of MADs. The study of the influence of all these effects on observed quantities goes beyond the scope of the present work. The current simulation set constitutes a reference point for future investigations.

¹ The authors thank Maciek Wielgus for providing ALMA data and comments on the paper. We also thank Andrew Chael, Charles Gammie, and Ben Ryan for many of their comments. We gratefully acknowledge the HPC RIVR consortium (www.hpc-rivr.si) and EuroHPC JU (eurohpc-ju.europa.eu) for funding this research by providing the computing resources of the HPC system Vega at the Institute of Information Science (www.izum.si).

Software `ebhlight` (Ryan et al. 2015, 2017, 2018), `ipole` (Mościbrodzka & Gammie 2018), `python` (Oliphant 2007), `matplotlib` (Hunter 2007).

REFERENCES

- Anantua, R., Ressler, S., & Quataert, E. 2020, MNRAS, 493, 1404
- Chael, A., Narayan, R., & Johnson, M. D. 2019, MNRAS, 486, 2873
- Chael, A., Rowan, M., Narayan, R., Johnson, M., & Sironi, L. 2018, MNRAS, 478, 5209
- Chael, A. A., Narayan, R., & Sadowski, A. 2017, MNRAS, 470, 2367
- Chan, C.-K., Psaltis, D., Özel, F., Narayan, R., & Sadowski, A. 2015, ApJ, 799, 1
- Chan, H.-S., Chan, C.-k., Prather, B. S., Wong, G. N., & Gammie, C. 2024, ApJ, 964, 17
- Chatterjee, K., Younsi, Z., Liska, M., et al. 2020, MNRAS, 499, 362
- Cruz-Osorio, A., Fromm, C. M., Mizuno, Y., et al. 2022, Nature Astronomy, 6, 103
- Davelaar, J., Mościbrodzka, M., Bronzwaer, T., & Falcke, H. 2018, A&A, 612, A34
- Davelaar, J., Olivares, H., Porth, O., et al. 2019, A&A, 632, A2
- Dexter, J., Jiménez-Rosales, A., Ressler, S. M., et al. 2020a, MNRAS, 494, 4168
- Dexter, J., Tchekhovskoy, A., Jiménez-Rosales, A., et al. 2020b, MNRAS, 497, 4999
- Dihingia, I. K., Mizuno, Y., Fromm, C. M., & Rezzolla, L. 2023, MNRAS, 518, 405
- Dolence, J. C., Gammie, C. F., Mościbrodzka, M., & Leung, P. K. 2009, ApJS, 184, 387
- Emami, R., Anantua, R., Chael, A. A., & Loeb, A. 2021, ApJ, 923, 272
- Event Horizon Telescope Collaboration, Akiyama, K., Alberdi, A., et al. 2022, ApJL, 930, L16
- Event Horizon Telescope Collaboration, Akiyama, K., Algaba, J. C., et al. 2021, ApJL, 910, L13
- Fishbone, L. G. & Moncrief, V. 1976, ApJ, 207, 962
- Foucart, F., Chandra, M., Gammie, C. F., Quataert, E., & Tchekhovskoy, A. 2017, MNRAS, 470, 2240
- Fromm, C. M., Cruz-Osorio, A., Mizuno, Y., et al. 2022, A&A, 660, A107
- Galishnikova, A., Philippov, A., & Quataert, E. 2023, ApJ, 957, 103
- Gammie, C. F., McKinney, J. C., & Tóth, G. 2003, ApJ, 589, 444
- Gold, R., McKinney, J. C., Johnson, M. D., & Doeleman, S. S. 2017, ApJ, 837, 180
- Howes, G. G. 2010, MNRAS, 409, L104
- Hunter, J. D. 2007, Computing in Science and Engineering, 9, 90
- Igumenshchev, I. V., Narayan, R., & Abramowicz, M. A. 2003, ApJ, 592, 1042
- Jiang, H.-X., Mizuno, Y., Fromm, C. M., & Nathaniel, A. 2023, MNRAS, 522, 2307
- Kawazura, Y., Barnes, M., & Schekochihin, A. A. 2019, Proceedings of the National Academy of Science, 116, 771
- Kim, J. Y., Krichbaum, T. P., Lu, R. S., et al. 2018, A&A, 616, A188
- Livadiotis, G., Desai, M. I., & Wilson, L. B., I. 2018, ApJ, 853, 142
- McKinney, J. C., Tchekhovskoy, A., & Blandford, R. D. 2012, MNRAS, 423, 3083
- Mizuno, Y., Fromm, C. M., Younsi, Z., et al. 2021, MNRAS, 506, 741
- Mościbrodzka, M. & Falcke, H. 2013, A&A, 559, L3

- Mościbrodzka, M., Falcke, H., & Shiokawa, H. 2016, A&A, 586, A38
- Mościbrodzka, M., Falcke, H., Shiokawa, H., & Gammie, C. F. 2014, A&A, 570, A7
- Mościbrodzka, M. & Gammie, C. F. 2018, MNRAS, 475, 43
- Mościbrodzka, M. & Gammie, C. F. 2024, ApJ, 968, 6
- Mościbrodzka, M., Gammie, C. F., Dolence, J. C., & Shiokawa, H. 2011, ApJ, 735, 9
- Narayan, R., Chael, A., Chatterjee, K., Ricarte, A., & Curd, B. 2022, MNRAS, 511, 3795
- Narayan, R., Igumenshchev, I. V., & Abramowicz, M. A. 2003, PASJ, 55, L69
- Oliphant, T. E. 2007, Computing in Science and Engineering, 9, 10
- Palumbo, D. C. M., Wong, G. N., & Prather, B. S. 2020, ApJ, 894, 156
- Pandya, A., Zhang, Z., Chandra, M., & Gammie, C. F. 2016, ApJ, 822, 34
- Petersen, E. & Gammie, C. 2020, MNRAS, 494, 5923
- Porth, O., Mizuno, Y., Younsi, Z., & Fromm, C. M. 2021, MNRAS, 502, 2023
- Proga, D. & Begelman, M. C. 2003, ApJ, 592, 767
- Ressler, S. M., Quataert, E., & Stone, J. M. 2019, MNRAS, 482, L123
- Ressler, S. M., Tchekhovskoy, A., Quataert, E., Chandra, M., & Gammie, C. F. 2015, MNRAS, 454, 1848
- Ressler, S. M., Tchekhovskoy, A., Quataert, E., & Gammie, C. F. 2017, MNRAS, 467, 3604
- Ricarte, A., Gammie, C., Narayan, R., & Prather, B. S. 2023, MNRAS, 519, 4203
- Rowan, M. E., Sironi, L., & Narayan, R. 2017, ApJ, 850, 29
- Ryan, B. R., Dolence, J. C., & Gammie, C. F. 2015, ApJ, 807, 31
- Ryan, B. R., Ressler, S. M., Dolence, J. C., Gammie, C., & Quataert, E. 2018, ApJ, 864, 126
- Ryan, B. R., Ressler, S. M., Dolence, J. C., et al. 2017, ApJL, 844, L24
- Sadowski, A., Wielgus, M., Narayan, R., et al. 2017, MNRAS, 466, 705
- Salas, L., Liska, M., Markoff, S., et al. 2024, arXiv e-prints, arXiv:2411.09556
- Scepi, N., Dexter, J., & Begelman, M. C. 2022, MNRAS, 511, 3536
- Tchekhovskoy, A., Narayan, R., & McKinney, J. C. 2011, MNRAS, 418, L79
- Vos, J. T., Olivares, H., Cerutti, B., & Mościbrodzka, M. 2024, MNRAS, 531, 1554
- Walker, R. C., Hardee, P. E., Davies, F. B., Ly, C., & Junor, W. 2018, ApJ, 855, 128
- Wielgus, M., Issaoun, S., Martí-Vidal, I., et al. 2024, A&A, 682, A97
- Wielgus, M., Marchili, N., Martí-Vidal, I., et al. 2022a, ApJL, 930, L19
- Wielgus, M., Moscibrodzka, M., Vos, J., et al. 2022b, A&A, 665, L6
- Wong, G. N. & Gammie, C. F. 2022, ApJ, 937, 60
- Xiao, F. 2006, Plasma Physics and Controlled Fusion, 48, 203
- Yfantis, A. I., Mościbrodzka, M. A., Wielgus, M., Vos, J. T., & Jimenez-Rosales, A. 2024, A&A, 685, A142
- Zhao, S.-S., Huang, L., Lu, R.-S., & Shen, Z. 2023, MNRAS, 519, 340

a_*	ID	R_{low}	R_{high}	i	$\frac{\dot{M}}{10^{17}}$	$\langle \dot{M} \rangle$	t_s	t_f	Δt	Resolution	Cooling
				(deg)		(M_\odot/yr)	(M)	(M)	(M)		
Convergence Study Models											
0	K_HHR	-	-	160	5	1.0×10^{-8}	5000	10,000	10	$360 \times 120 \times 192$	no
0	K_HR	-	-	160	5	1.1×10^{-8}	5000	10,000	10	$240 \times 240 \times 128$	no
0	K_MR	-	-	160	5	1.0×10^{-8}	5000	10,000	10	$240 \times 120 \times 128$	no
0	K_LR	-	-	160	5	1.2×10^{-8}	5000	10,000	10	$120 \times 120 \times 128$	no
Fiducial Models											
-0.9375	K	-	-	160	2	4.6×10^{-9}	10,000	14,000	10	$266 \times 120 \times 128$	No
-0.9375	K	-	-	150	2	4.6×10^{-9}	10,000	14,000	10	$266 \times 120 \times 128$	No
-0.9375	K	-	-	130	2	4.6×10^{-9}	10,000	14,000	10	$266 \times 120 \times 128$	No
-0.9375	K	-	-	110	2	4.6×10^{-9}	10,000	14,000	10	$266 \times 120 \times 128$	No
-0.5	K	-	-	160	5	6.9×10^{-9}	10,000	14,000	10	$240 \times 120 \times 128$	No
-0.5	K	-	-	150	4.5	6.2×10^{-9}	10,000	14,000	10	$240 \times 120 \times 128$	No
-0.5	K	-	-	130	4	5.5×10^{-9}	10,000	14,000	10	$240 \times 120 \times 128$	No
-0.5	K	-	-	110	4	5.5×10^{-9}	10,000	14,000	10	$240 \times 120 \times 128$	No
0	R1	1	1	160	3	4.2×10^{-9}	15,000	30,000	10	$240 \times 120 \times 128$	No
0	R10	1	10	160	5	7×10^{-9}	15,000	30,000	10	$240 \times 120 \times 128$	No
0	R40	1	40	160	7	9.8×10^{-9}	15,000	30,000	10	$240 \times 120 \times 128$	No
0	R160	1	160	160	10	1.4×10^{-8}	15,000	30,000	10	$240 \times 120 \times 128$	No
0	K	-	-	160	5	7×10^{-9}	15,000	30,000	10	$240 \times 120 \times 128$	No
0	K	-	-	150	5	7×10^{-9}	15,000	30,000	10	$240 \times 120 \times 128$	No
0	K	-	-	130	4	5.6×10^{-9}	15,000	30,000	10	$240 \times 120 \times 128$	No
0	K	-	-	110	4	5.6×10^{-9}	15,000	30,000	10	$240 \times 120 \times 128$	No
0.5	R1-160	1	1	160	2	2.7×10^{-9}	15,000	30,000	10	$240 \times 120 \times 128$	No
0.5	R10	1	10	160	3	4.1×10^{-9}	15,000	30,000	10	$240 \times 120 \times 128$	No
0.5	R40	1	40	160	5	6.9×10^{-9}	15,000	30,000	10	$240 \times 120 \times 128$	No
0.5	R160	1	160	160	8	1.1×10^{-8}	15,000	30,000	10	$240 \times 120 \times 128$	No
0.5	K	-	-	160	3	4.1×10^{-9}	15,000	30,000	10	$240 \times 120 \times 128$	No
0.5	K	-	-	150	3	4.1×10^{-9}	15,000	30,000	10	$240 \times 120 \times 128$	No
0.5	K	-	-	130	3	4.1×10^{-9}	15,000	30,000	10	$240 \times 120 \times 128$	No
0.5	K	-	-	110	3	4.1×10^{-9}	15,000	30,000	10	$240 \times 120 \times 128$	No
0.9375	R1	1	1	160	1.5	2.0×10^{-9}	15,000	30,000	10	$266 \times 120 \times 128$	No
0.9375	R10	1	10	160	2	2.7×10^{-9}	15,000	30,000	10	$266 \times 120 \times 128$	No
0.9375	R40	1	40	160	4	5.5×10^{-9}	15,000	30,000	10	$266 \times 120 \times 128$	No
0.9375	R160	1	160	160	6	8.3×10^{-9}	15,000	30,000	10	$266 \times 120 \times 128$	No
0.9375	K	-	-	160	2	2.7×10^{-9}	15,000	30,000	10	$266 \times 120 \times 128$	No
0.9375	K	-	-	150	2	2.7×10^{-9}	15,000	30,000	10	$266 \times 120 \times 128$	No
0.9375	K	-	-	130	2	2.7×10^{-9}	15,000	30,000	10	$266 \times 120 \times 128$	No
0.9375	K	-	-	110	2	2.7×10^{-9}	15,000	30,000	10	$266 \times 120 \times 128$	No
Exploratory Models											
0	K, cooling	-	-	-	5	8×10^{-9}	15,000	30,000	10	$240 \times 120 \times 128$	Yes
0.5	K, nonthermal	-	-	160	3	4.1×10^{-9}	15,000	30,000	10	$240 \times 120 \times 128$	No
0.5	K, nonthermal	-	-	150	3	4.1×10^{-9}	15,000	30,000	10	$240 \times 120 \times 128$	No
0.5	K, nonthermal	-	-	130	3	4.1×10^{-9}	15,000	30,000	10	$240 \times 120 \times 128$	No
0.5	K, nonthermal	-	-	110	3	4.1×10^{-9}	15,000	30,000	10	$240 \times 120 \times 128$	No

Table 1. List of GRMHD/GRRMHD and radiative transfer models resulting in different time series of images. Note. Accretion rates \dot{M} are time averages between t_s and t_f .

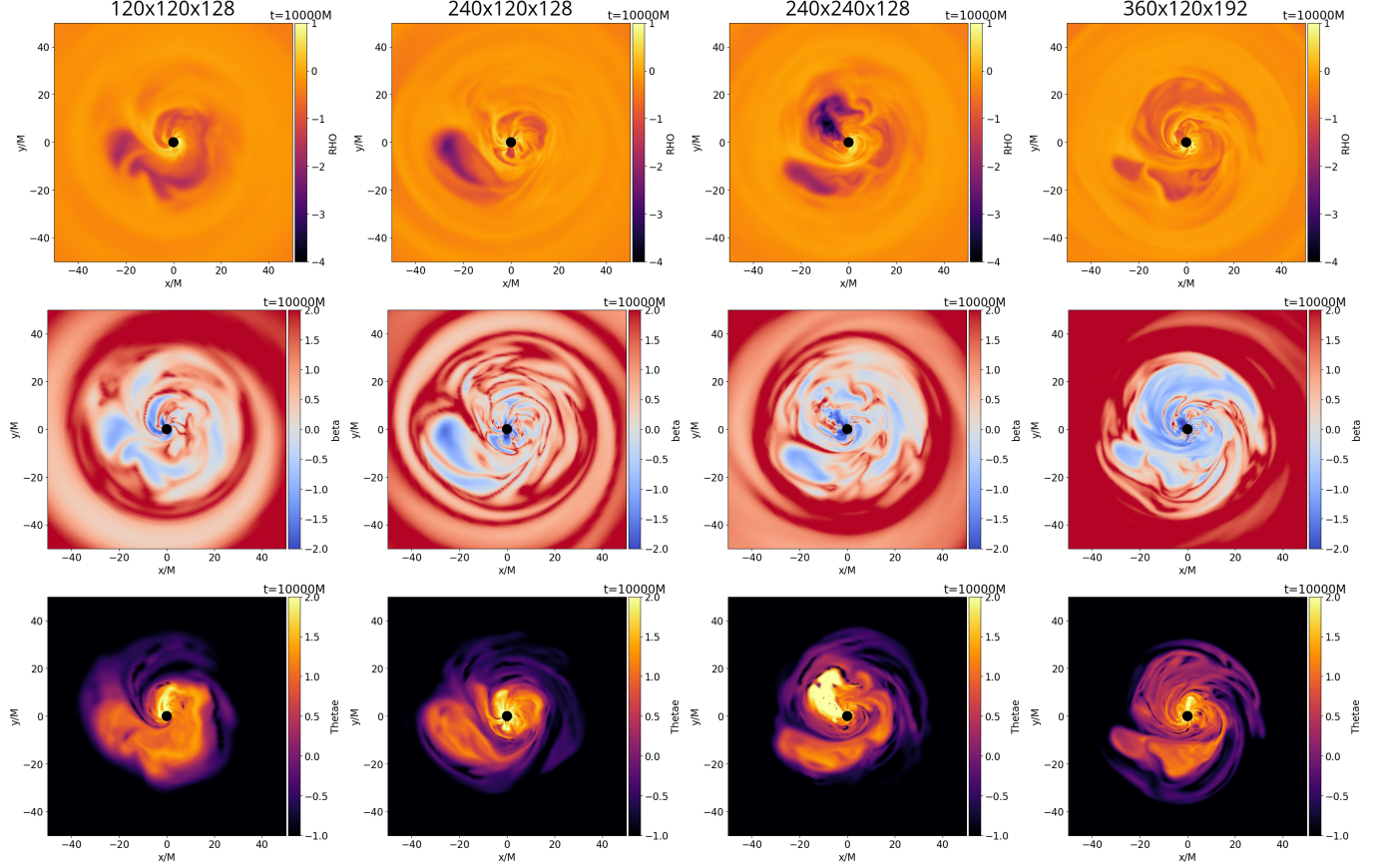


Figure 1. Equatorial density (top panels), plasma β (middle panels), and K model electron temperature (bottom panels) maps in various-resolution two-temperature MAD $a_* = 0$ models at $t = 10,000M$.

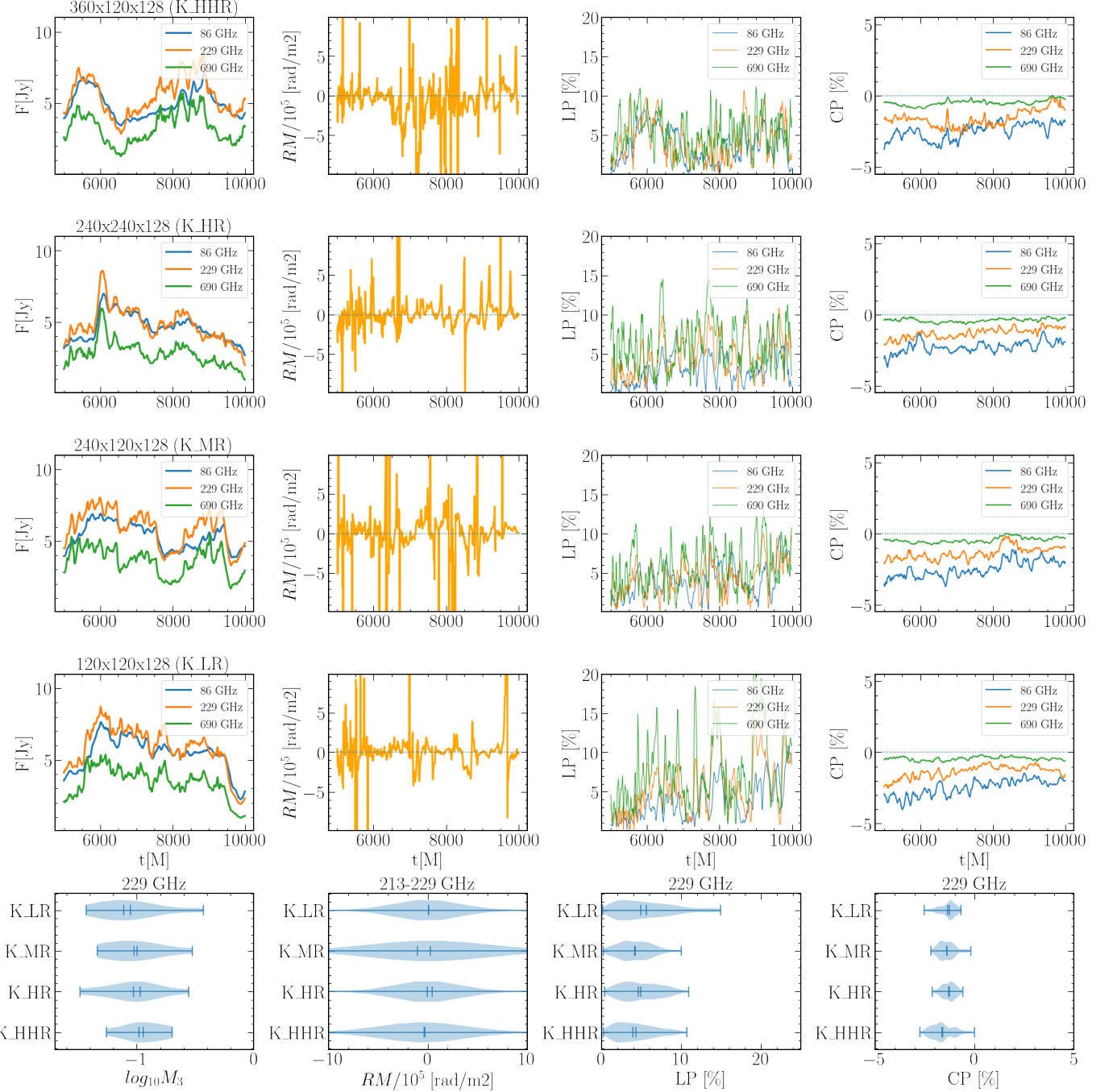


Figure 2. Comparison of Stokes I , RM, LP, and CP in two-temperature MAD $a_* = 0$ models with increasing grid resolution (Table 1). The vertical bars in the violin plots mark mean, median, and upper/lower limits of the distribution.

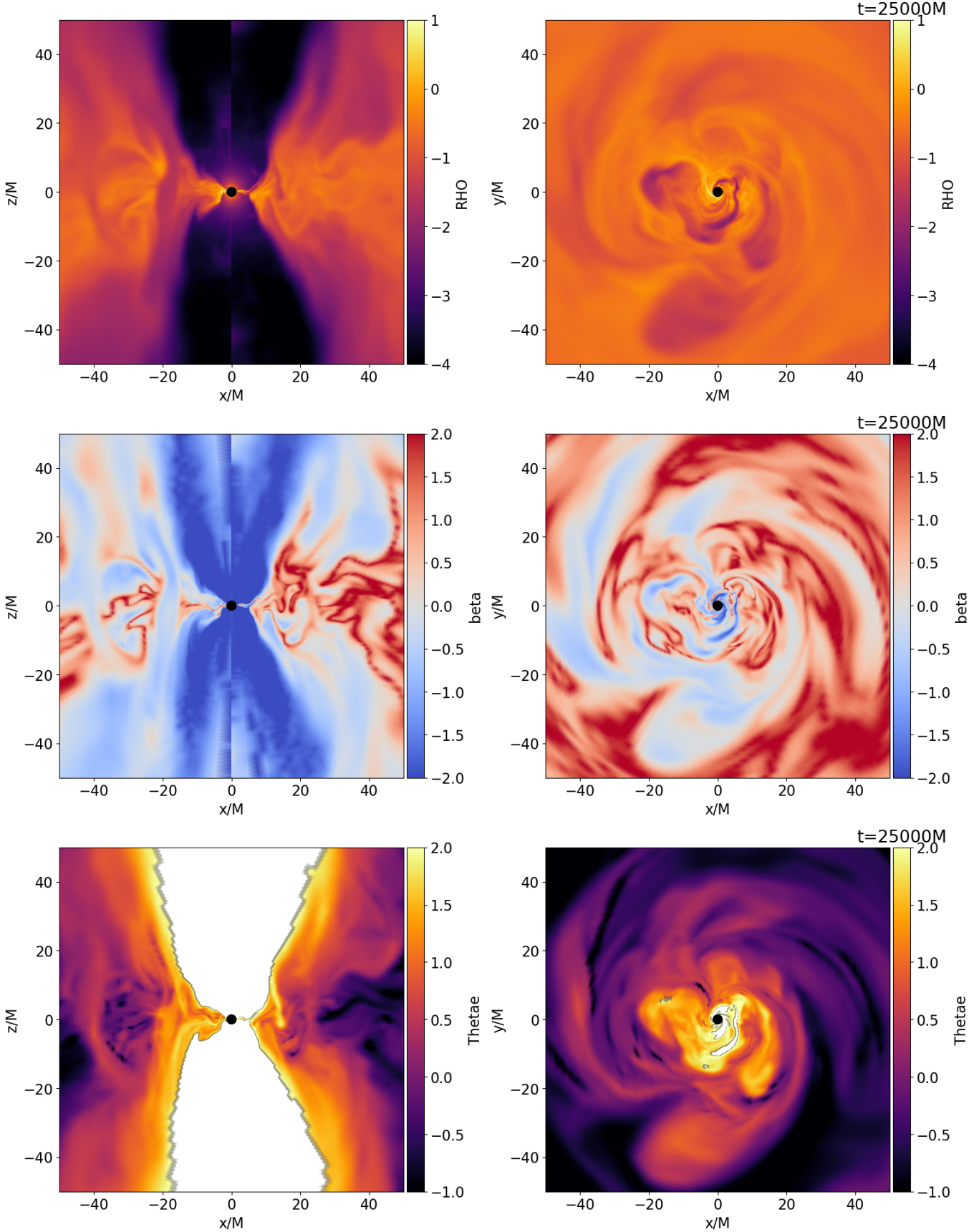


Figure 3. Examples of meridional and equatorial slices showing plasma density (top panels), plasma β parameter (middle panels) and K model electron temperatures (bottom panels) in the fiducial MAD $a_* = 0.9375$ simulation at $t = 25,000M$ (see Table 1). The panel with electron temperature masks the uncertain region not taken into account in radiative transfer calculations.

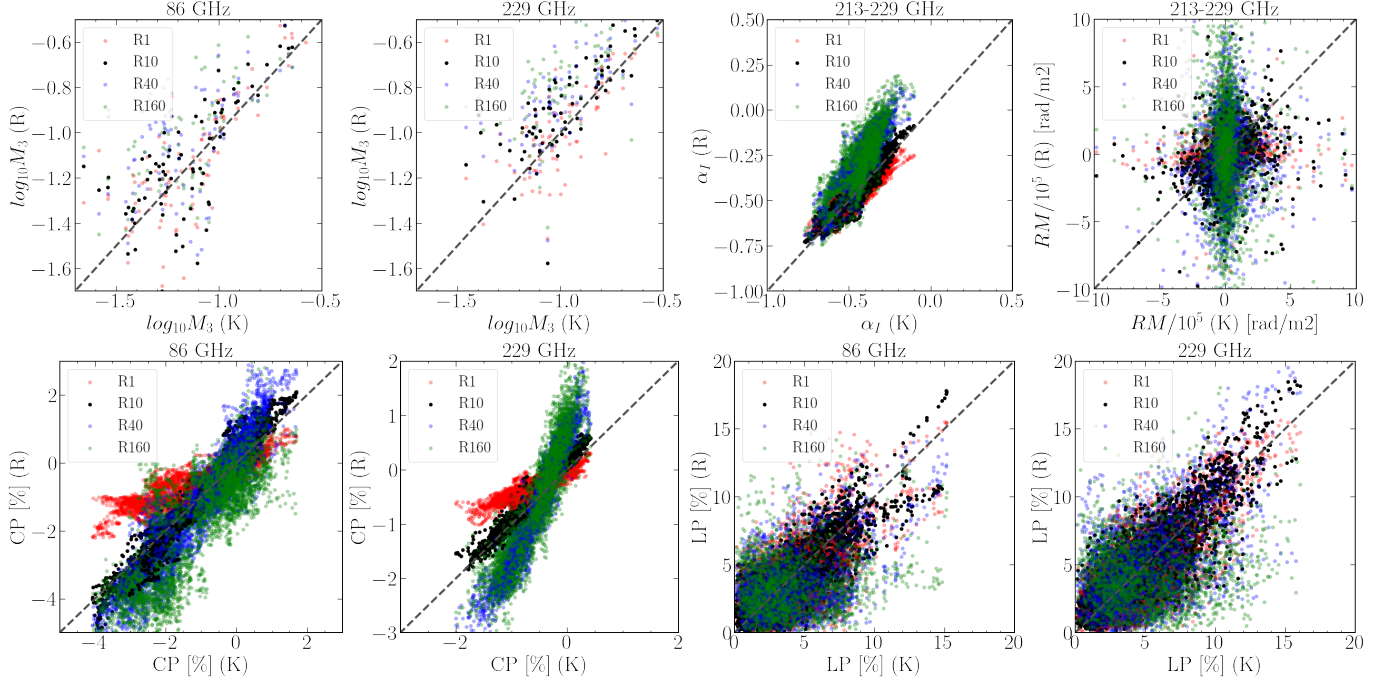


Figure 4. Comparison of the net radiative properties for MAD K and R1 - 160 (spins $a_* = 0, 0.5, 0.9375$ combined) models calculated for the default viewing angle $i = 160^\circ$. Top panels show modulation indices of Stokes I light curves at 86 and 229 GHz and spectral slopes and RM distributions around 229 GHz. In the bottom panels, we show distribution of fractional CP and LP polarizations for 86 and 229 GHz. All net quantities are built based on light curves from 15,000 to 30,000M.

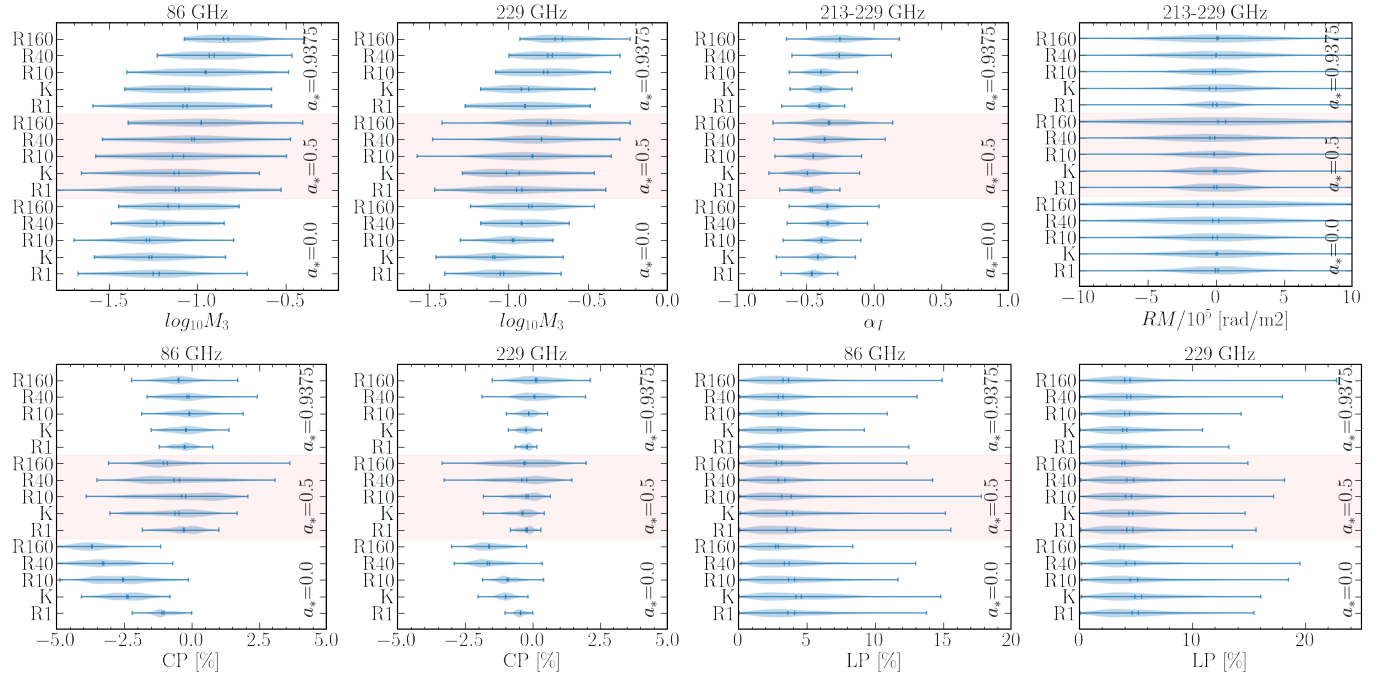


Figure 5. Comparison of distributions of various observables in MAD models K and R1 - 160 observed at $i = 160^\circ$. The light red background is introduced to visually separate models with different spins ($a_* = 0, 0.5, 0.9375$).

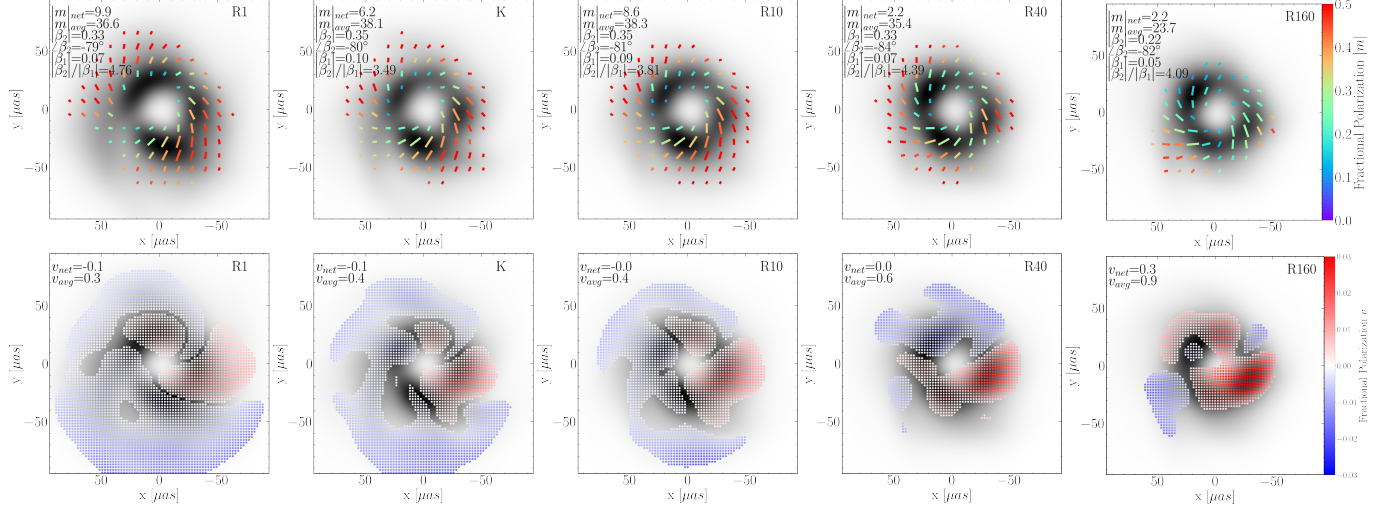


Figure 6. Comparison of snapshot images of MAD $a_* = 0.5$ models K, R1, R10, R40 and R160 at frequency of 229 GHz for the fiducial viewing angle $i = 160^\circ$. Images are blurred by a Gaussian kernel with FWHM = 20 μas to imitate the resolution of EHT. In the top panels, the gray scale is used for total intensity, and color ticks illustrate the LP of the emission. The linearly polarized fraction of total intensity is marked with color, and tick length is proportional to $P \equiv \sqrt{Q^2 + U^2}$. We do not show LP in regions where flux in P drops below 20% of its maximum. In the bottom panels, the fractional CP is plotted as points. We do not show CP in regions where $|V|$ drops below 5% of its maximum. K models are close to R10 models, but the details of the polarimetric characteristics are slightly different.

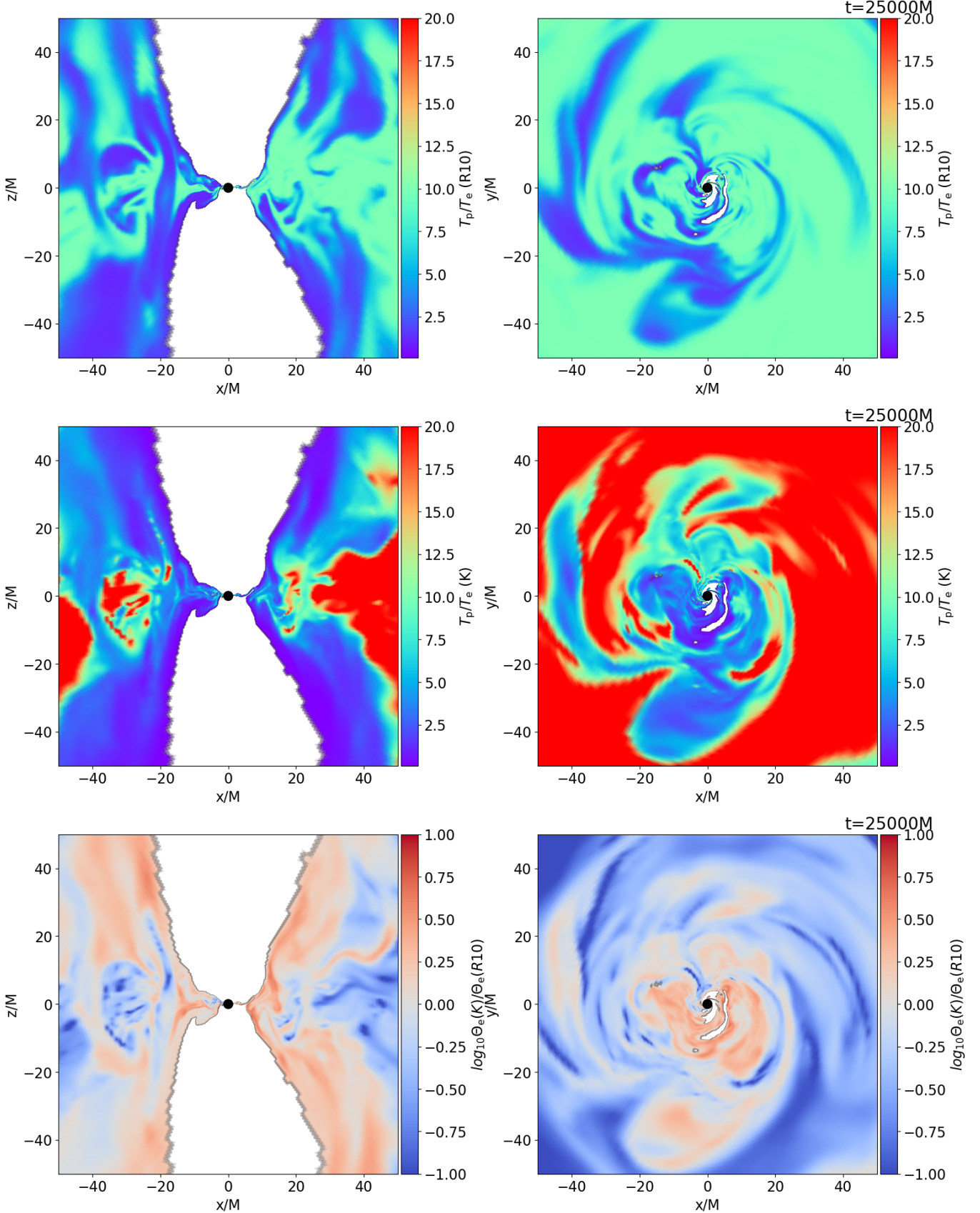


Figure 7. Examples of meridional and equatorial slices showing T_p/T_e (top panels show T_p/T_e in model R10 and middle panels show T_p/T_e in model K) and the ratio of K and R10 Θ_e (bottom panels) in MAD $a_* = 0.9375$ at $t = 25,000M$. The uncertain regions, not taken into account in radiative transfer calculations, are masked.

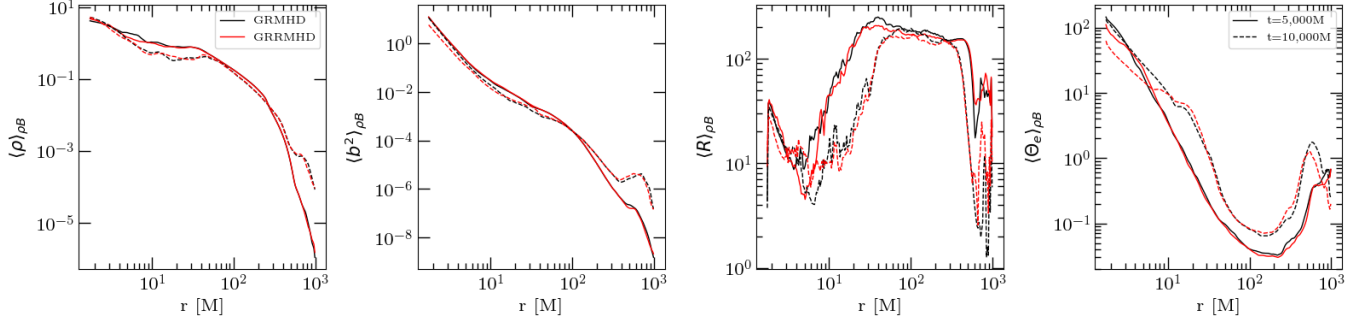


Figure 8. Comparison of radial profiles of density, magnetic field strength (square), proton-to-electron temperature ratio (R) and electron temperatures in GRMHD (black lines) and GRRMHD (red lines) models. All quantities are dimensionless or in code units, and they are all angle-averaged, where averaging of a quantity Q is defined as $\langle Q(r, t) \rangle \equiv \int_0^{2\pi} \int_0^\pi Q(r, \theta, \phi, t) \sqrt{-g} d\theta d\phi / \int_0^{2\pi} \int_0^\pi \sqrt{-g} d\theta d\phi$ where g is the metric determinant. All quantities are also weighted with the ρB factor to show quantities averaged over regions where most of the synchrotron emission comes from. Different line styles correspond to different time moments of the MAD evolution.

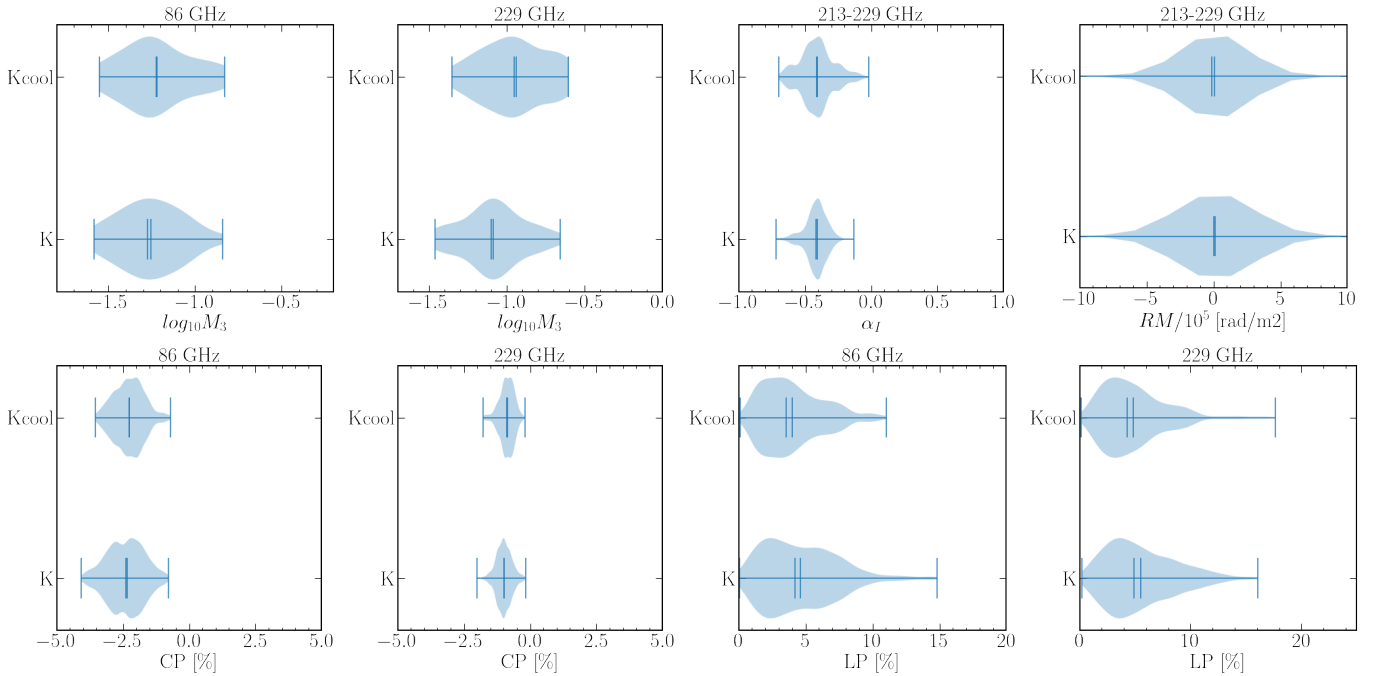


Figure 9. Comparison of radiative characteristics of the GRMHD (K) and GRRMHD (Kcool) models with $a_* = 0$ spin computed for light curves in the time interval $15,000 - 30,000M$.

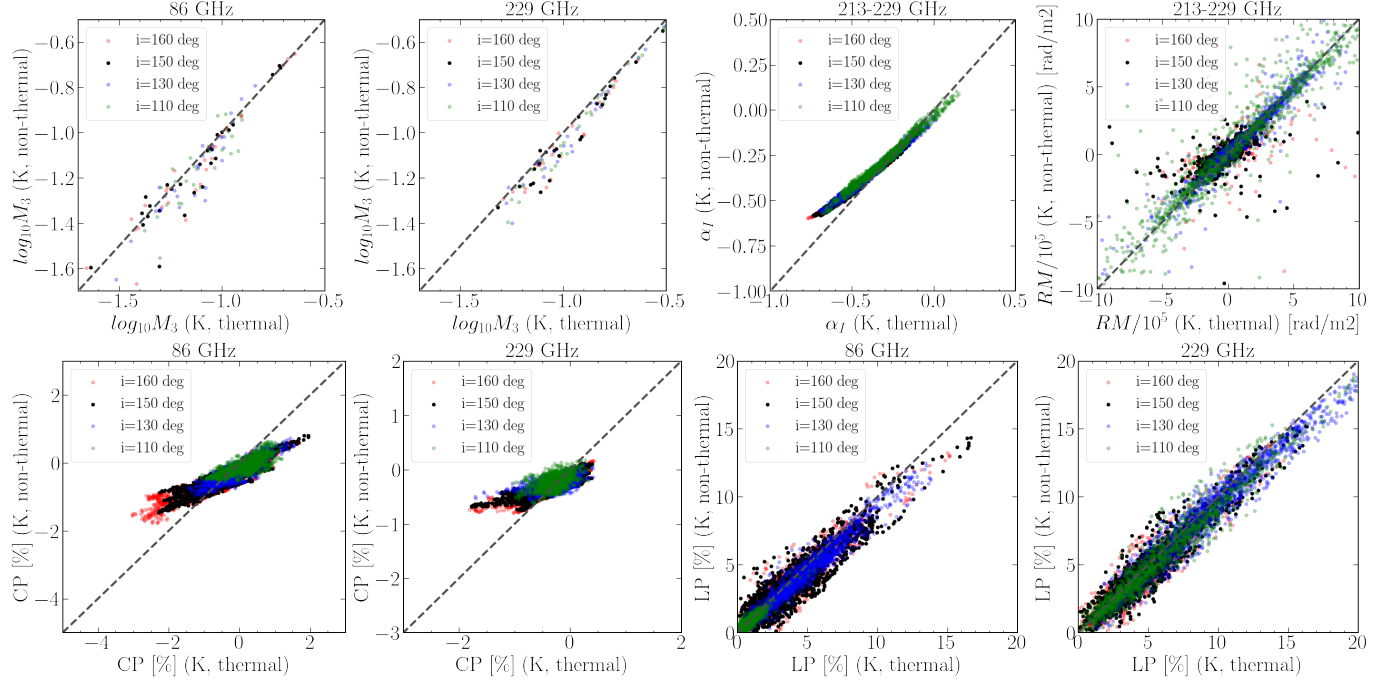


Figure 10. Comparison of the radiative characteristics of thermal and nonthermal MAD models with $a_* = 0.5$. All panels are the same as in Figure 4 but the colors indicate models with different viewing angles rather than different R_{high} parameters.

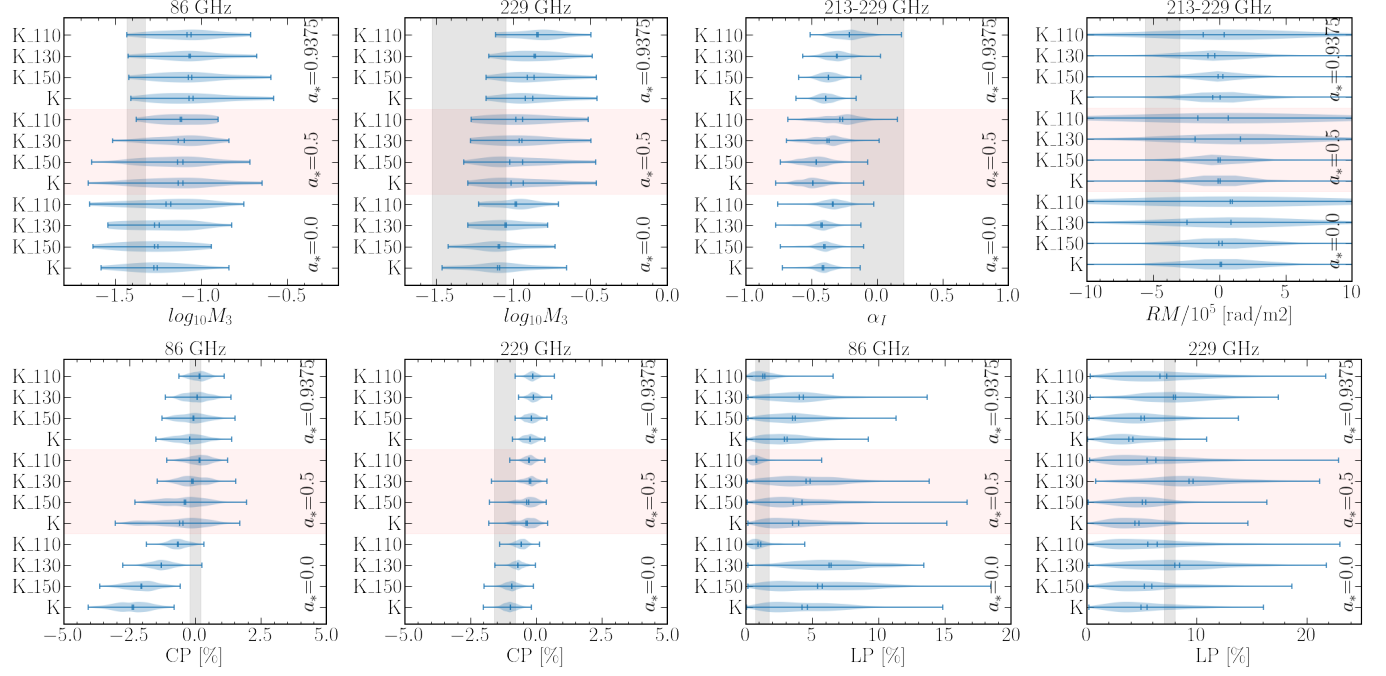


Figure 11. Comparison of radiative characteristics of MAD models K ($a_* = 0, 0.5, 0.9375$) at a default viewing angle of $i = 160^\circ$ (K) and three additional angles $i = 150^\circ, 130^\circ, 110^\circ$ deg (K_150, K_130, K_110) to observations of Sgr A* collected by ALMA in April 2017 (86 GHz data collected on April 3rd and 230 GHz data collected on April 6-11) and presented in Wielgus et al. (2022a,b, 2024) (gray bands). The light red background is introduced to visually separate models with different spins.

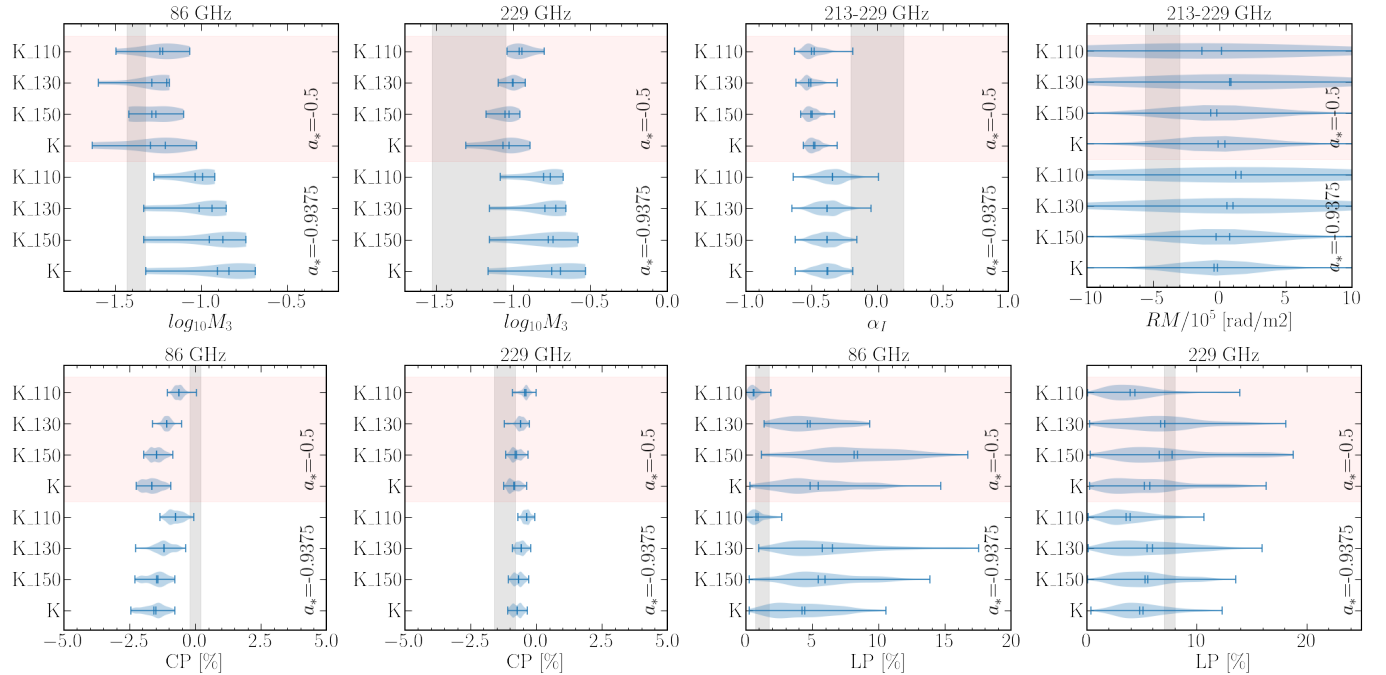


Figure 12. Same as Figure 11 but for retrograde models K.

APPENDIX

A. LIGHT CURVES

The main text of this manuscript presents statistical properties of light curves from MAD simulations with different spin values. Figures 13 - 15 present light curves of individual zero and prograde models for the default viewing angle $i = 160^\circ$. Here in addition to 86 and 229 GHz we also show light curves at 690 GHz for visual comparison.

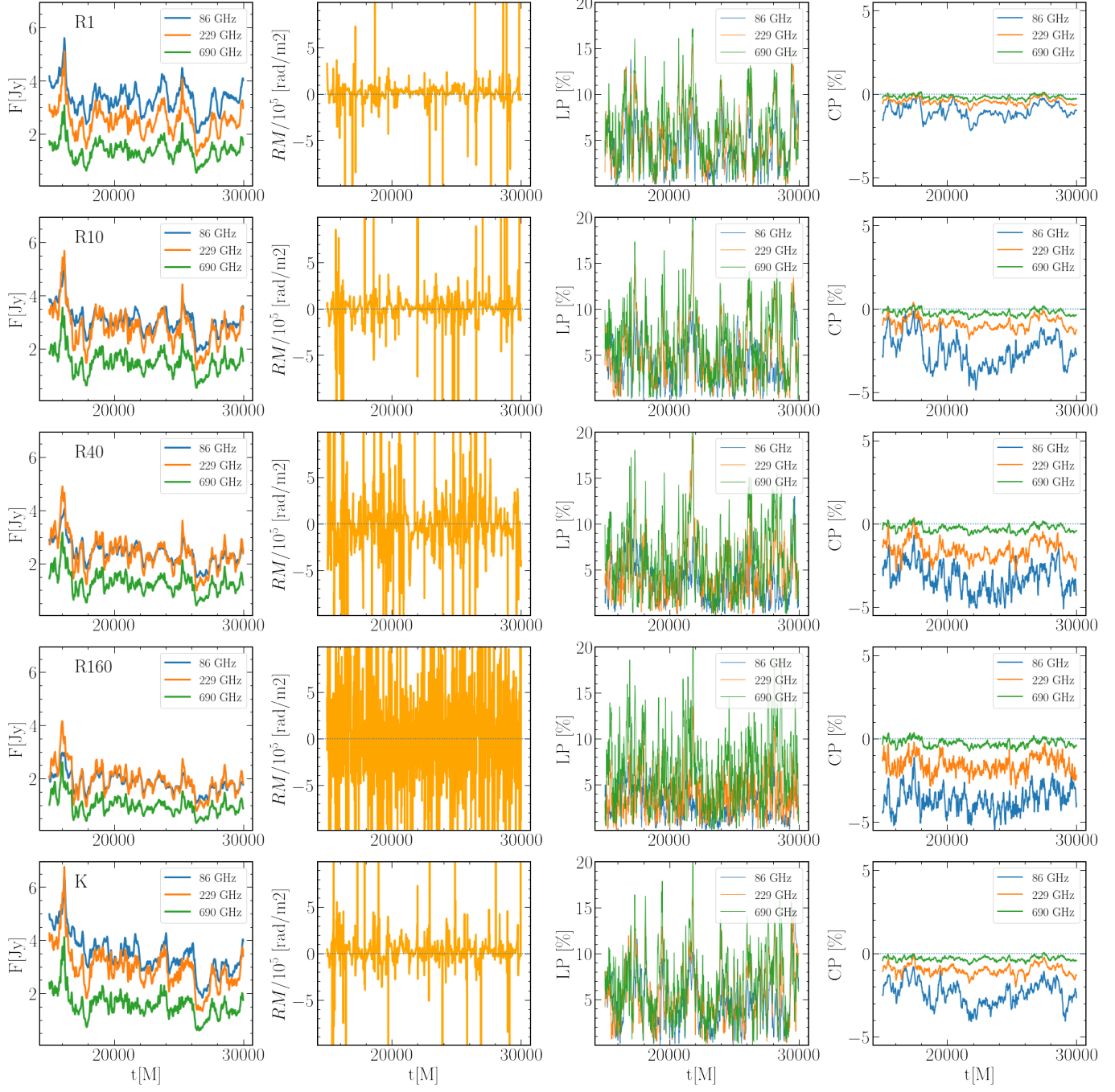


Figure 13. Radiative signatures for the MAD $a_* = 0$ model at the default viewing angle of $i = 160^\circ$. Panels from left to right display Stokes I (86, 229, 690 GHz), RM (213 - 229 GHz), LP (86, 229, 690 GHz) and CP (86, 229, 690 GHz). Panels from top to bottom show models R1-160, and K.



Figure 14. Same as in Figure 13 but for MAD $a_* = 0.5$ models R1 - 160 and K.

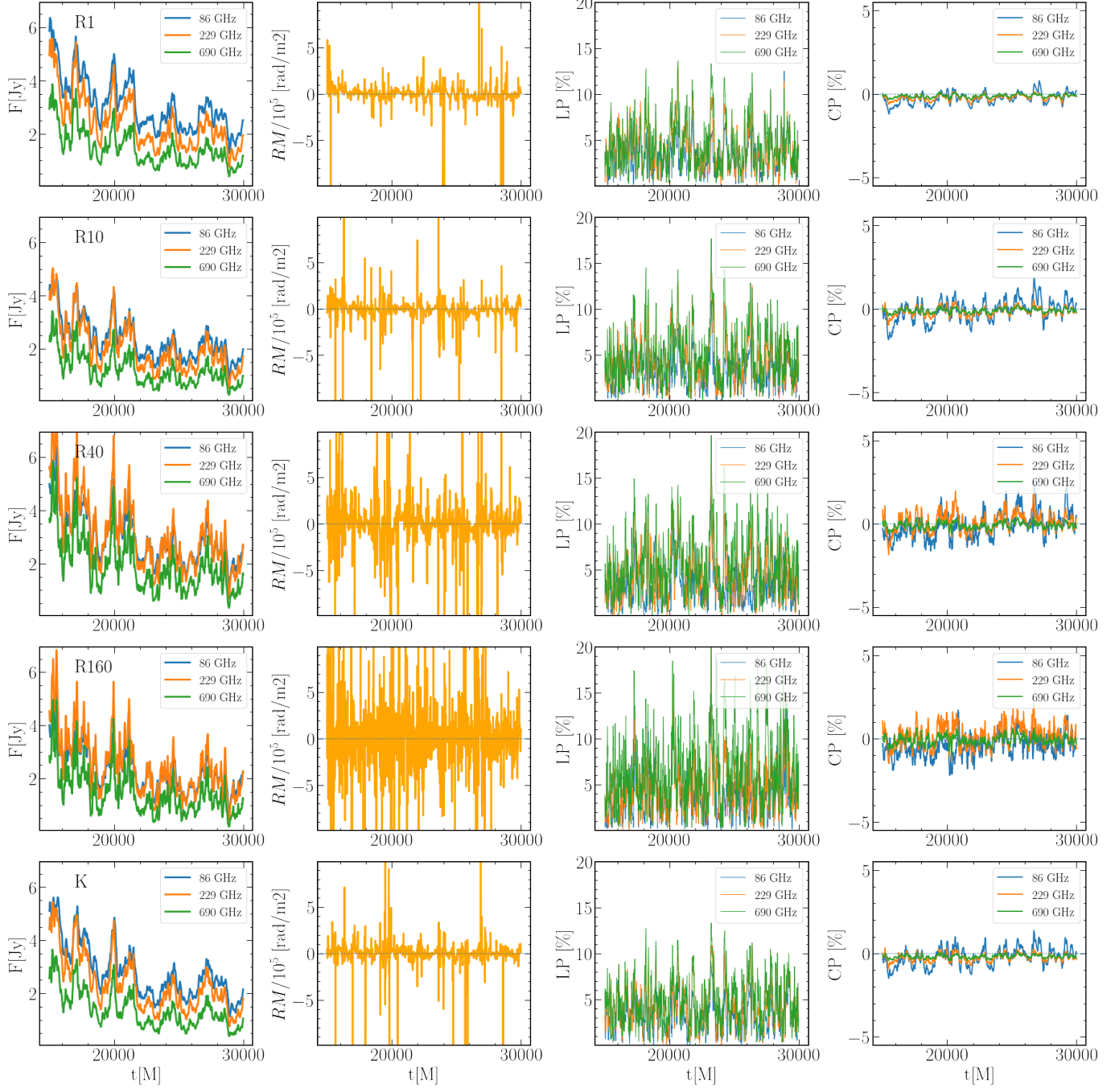


Figure 15. Same as in Figure 13 but for MAD $a_* = 0.94$ models R1 - 160 and K.

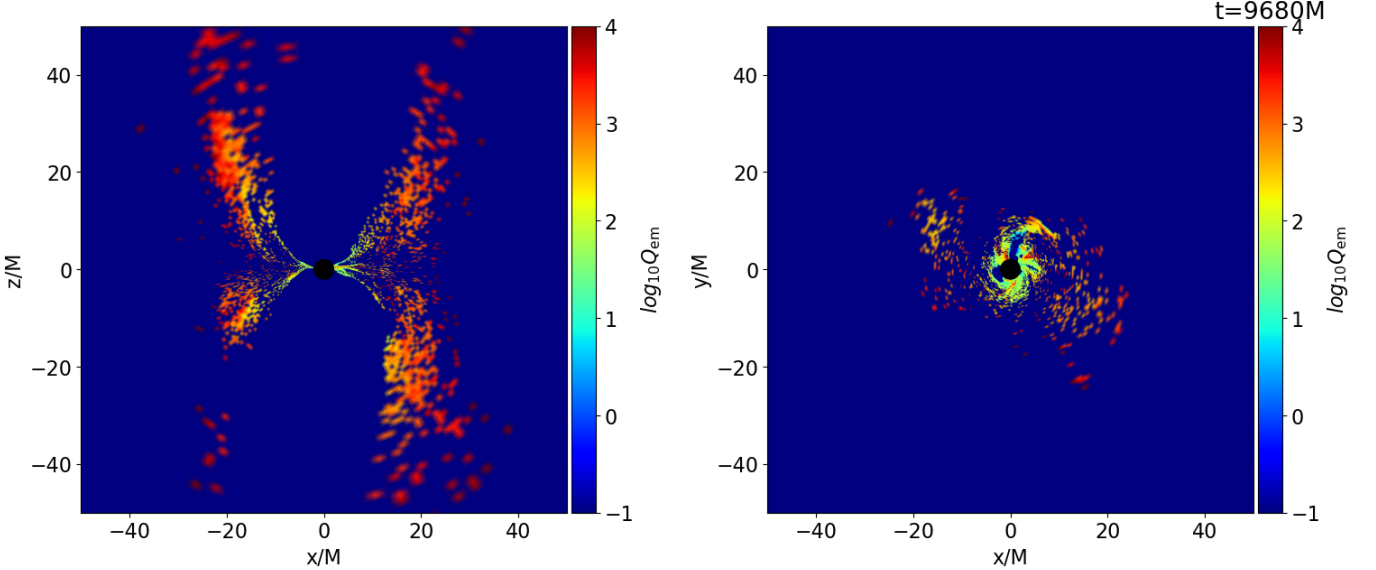


Figure 16. Meridional and equatorial slices showing number of superphotons emitted within one synchrotron cooling timescale in GRRMHD MAD $a_* = 0$ model. The figure illustrates not only the quality of the GRRMHD model but also the origin of the synchrotron emission in the two-temperature MAD models.

B. GRRMHD

In `ebhlight`, the multifrequency radiative transport is carried out using the Monte Carlo scheme in which the radiation field is simulated with a large number of superphoton particles representing an even larger number of physical photons (see code description in Ryan et al. 2015 for exact definitions). To make sure that the radiative cooling of plasma is well captured, for each fluid element, the Monte Carlo scheme has to produce a sufficient number of photon particles within the electron cooling timescale.

The electron cooling timescale (in M units) can be written as

$$\tau_{\text{cool}} = \frac{u_{e,\text{code}}}{\Lambda_{\text{code}}} \quad (\text{B1})$$

where $u_{e,\text{code}}$ is the electron internal energy provided by the two-temperature model (in code units) and where Λ_{code} is the synchrotron cooling rate (also in code units). In cgs units the cooling rate reads (Eq. (A4) from Mościbrodzka et al. 2011)

$$\Lambda_{\text{c.g.s.}} = \frac{16B^2e^4n_e\Theta_e^2}{3c^3m_e^2}. \quad (\text{B2})$$

where the conversion to code units is $\Lambda_{\text{code}} = \Lambda_{\text{cgs}}\mathcal{L}\mathcal{T}^3/\mathcal{M}$. Figure 16 shows the quality factor of GRRMHD Q_{em} , a number of superphotons emitted within τ_{cool} , for a snapshot of GRRMHD around $t = 10,000\text{M}$. $Q_{\text{em}} \gg 10$ in the inner disk ($r < 10\text{M}$) and along the jet wall, indicating reasonable sampling in regions where radiative cooling is the most efficient.

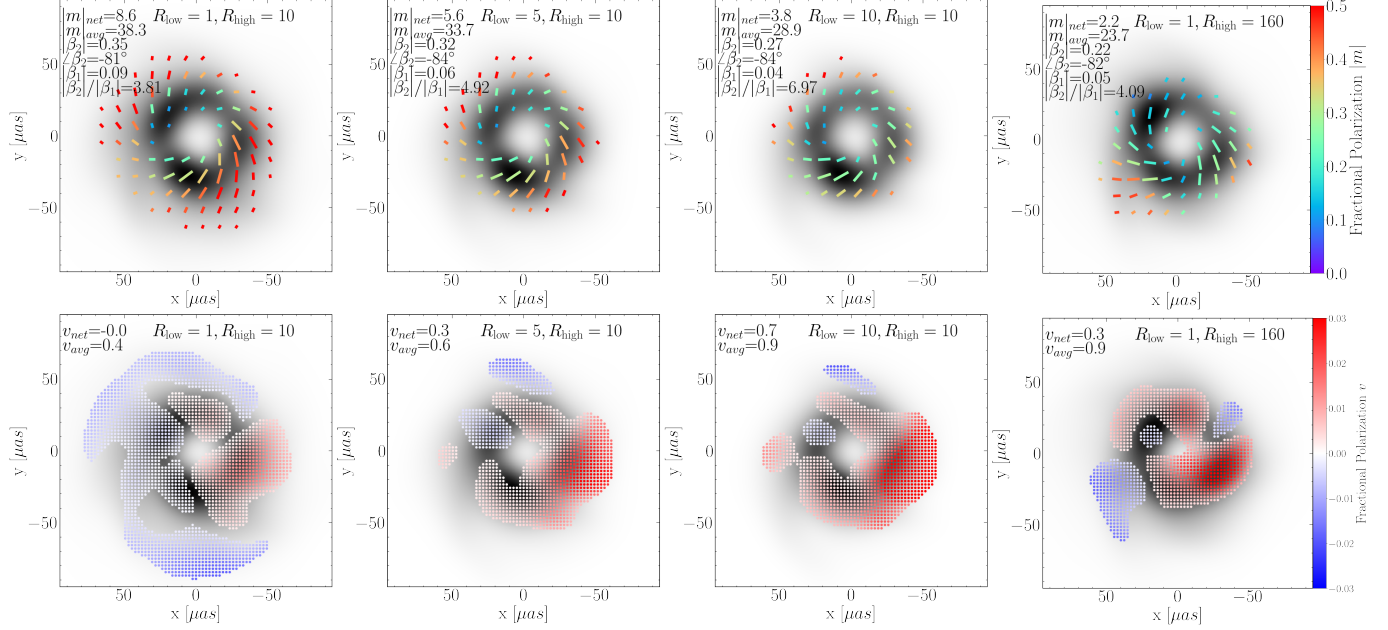


Figure 17. Polarimetric images of a single GRMHD MAD $a_* = 0.5$ snapshot. Panels show the same quantities as in Figure 6 but only for $R(\beta)$ models with different assumptions of R_{low} parameter in Equation 3. All models are normalized with different \mathcal{M} to reproduce the same total flux. From left to right: $\mathcal{M}/10^{17} = 3, 4, 5, 8$.

C. THE ISSUE OF R_{LOW} PARAMETER IN $R(\beta)$ MODEL AND PARAMETER INFERENCE

When estimating the parameters of the electron temperature using polarimetric images of Sgr A*, Event Horizon Telescope Collaboration et al. (2024) assumed that in Equation 3, $R_{\text{low}} = 1$. What happens if we relax the assumption about R_{low} ? Figure 17 shows the impact of the varying parameter R_{low} on the linear and circular polarimetric images of Sgr A*. The images of the MAD with $(R_{\text{low}}, R_{\text{high}}) = (10, 10)$ start to resemble those of $(R_{\text{low}}, R_{\text{high}}) = (1, 160)$. Therefore, it is possible that the polarimetric scoring of the models with $R_{\text{low}} \sim 10$ could lead to different best-fit values of $R_{\text{high}} \ll 160$. If this is indeed the case, which will have to be carefully verified in the future, estimations of the electron temperature parameters using $R(\beta)$ models with $R_{\text{low}} \sim 10$ have a better chance of convergence with some of the discussed Q_p^+/Q_e^+ models, proving that particle-in-cell models applied to GRMHD simulations correctly predict the order of magnitude of electron heating in collisionless plasma.